ANTTI AHO
OPTIMIZATION OF SEMICONDUCTOR OPTICAL AMPLIFIER LENGTH FOR MINIMUM POWER CONSUMPTION

Master of Science thesis

ABSTRACT

Semiconductor optical amplifiers (SOAs) are important optoelectronic components with many applications. This thesis focuses on the application of SOAs as integrated amplifiers in an optical interconnect system. In order to meet the amplification requirement of the application, SOAs of different lengths may be used and operated with different injection currents. Different component lengths result in varying power consumption which is wanted to be kept as low as possible. The aim of this thesis was to develop a method to find the optimal SOA length with the lowest power consumption.

The length optimization was performed by fabricating and characterizing ridge waveguide lasers with a geometry similar to that of the target SOAs. Three different parameters – operating voltage, modal gain and saturation power – and their dependence on the injection current density were determined. Antireflection coating using atomic layer deposition was applied to the components to obtain modal gain data at high injection current densities.

Two different SOA materials were studied: a novel GaInNAsSb/GaAs structure emitting around $1300\,\mathrm{nm}$ and a more traditional AlGaInAs/InP structure emitting around $1550\,\mathrm{nm}$.

The target application had four different operation cases with varying amplification targets. A component length resulting in the minimum power consumption was succesfully determined for all the cases and for both materials.

TIIVISTELMÄ

Optiset puolijohdevahvistimet ovat tärkeitä optoelektroniikan komponentteja, joilla on monia käyttökohteita. Tässä diplomityössä tarkastellaan näiden vahvistinten käyttöä integroituina vahvistimina optisessa linkkijärjestelmässä. Eripituiset vahvistimet voivat tuottaa järjestelmän vaatiman vahvistuksen, kun niitä käytetään erisuuruisilla sähkövirroilla, mutta myös tehonkulutus vaihtelee eri pituuksien välillä. Tämän diplomityön tavoitteena oli kehittää menetelmä, jolla voidaan laskea, mikä vahvistimen pituus mahdollistaa alhaisimman tehonkulutuksen.

Pituuden optimoinnissa käytettiin apuna harjanneaaltojohdelasereita, joiden rakenne oli samankaltainen kuin varsinaisilla vahvistimilla. Analyysiä varten selvitettiin kolmen parametrin – käyttöjännitteen, moodivahvistuksen ja saturaatiotehon – riippuvuus virrantiheydestä. Atomikerroskasvatuksella valmistettuja heijastusta pienentäviä kalvoja käytettiin moodivahvistusdatan saamiseksi suurilla virrantiheyksillä.

Diplomityössä tutkittiin kahta eri vahvistinmateriaalia. Fokus oli uudentyyppisellä GaInNAsSb/GaAs-puolijohderakenteella, jonka emissioaallonpituus oli noin 1300 nm. Vertailukohteena oli tavanomaisissa tiedonsiirtolasereissa käytetyn materiaalin kaltainen, aallonpituudella 1550 nm emittoiva AlGaInAs/InP-rakenne.

Kohdesovelluksessa oli neljä eri käyttötapaa ja vahvistusvaatimusta vahvistimille. Työssä onnistuttiin löytämään jokaiselle käyttötavalle ja molemmille materiaaleille vahvistimen pituus, joka tuotti pienimmän mahdollisen tehonkulutuksen.

PREFACE

This master's thesis has been done at the Optoelectronics Research Centre, Tampere University of Technology. I would like to thank ORC's management for offering me the opportunity to write this thesis as well as Ms. Anne Viherkoski and Ms. Eija Heliniemi for helping with the bureaucracy.

I wish to thank Dr. Jukka Viheriälä and Adj. Prof. Mihail Dumitrescu for acting as the examiners for my thesis. I'm also deeply grateful to Mr. Heikki Virtanen and Mr. Topi Uusitalo for their simulations that were essential to this thesis. I would like to thank Ms. Mariia Bister and Mr. Jaakko Mäkelä for the processing of the samples used in this thesis, as well as Mr. Petri Melanen and Modulight Inc. for performing the bar probing measurements. I wish to thank Dr. Kimmo Lahtonen and Mr. Jesse Saari for performing the ALD coatings.

I want to thank Mr. Joel Salmi for the interesting debates and facts, Mr. Riku Isoaho and Ms. Heidi Tuorila for the peer support during the writing of this thesis, Dr. Antti Härkönen for having an answer to just about any question that I have ever asked him, and Ms. Mervi Koskinen and the rest of ORC's processing team for their support. Finally I would like to thank all my co-workers at ORC – present, past, and late – for creating such a friendly and warm work environment.

Tampere, 21 June 2016

Antti T. Aho

TABLE OF CONTENTS

LIST OF PUBLICATIONS

[I] **Antti T. Aho**, Jukka Viheriälä, Ville-Markus Korpijärvi, Mervi Koskinen, Heikki Virtanen, Kimmo Lahtonen, Jesse Saari and Mircea Guina, "High-power GaInNAs distributed Bragg reflector laser diodes emitting at 1180 nm", under preparation

[II] Jukka Viheriälä, **Antti T. Aho**, Jaakko Mäkelä, Joel Salmi, Heikki Virtanen, Tomi Leinonen, Mihail Dumitrescu, and Mircea Guina, "High-power 1550 nm tapered DBR lasers fabricated using soft UV-nano-imprint lithography", Proc. SPIE 9733, High-Power Diode Laser Technology and Applications XIV, 97330Q (March 4, 2016)

[III] J. Viheriälä, J. Mäkelä, **A. Aho**, H. Virtanen, T. Leinonen, M. Dumitrescu, and M. Guina, "High-power 1550 nm tapered DBR lasers fabricated using soft UV-nanoimprint lithography," in 2015 European Conference on Lasers and Electro-Optics - European Quantum Electronics Conference, (Optical Society of America, 2015), paper CB_5_1.

[IV] J. Telkkälä, J. Viheriälä, **A. Aho**, P. Melanen, J. Karinen, M. Dumitrescu and M. Guina, "Narrow linewidth laterally-coupled 1.55 mm DFB lasers fabricated using nanoimprint lithography", Electronics Letters Vol. 47 No. 6, 2011

[V] Ville-Markus Korpijärvi, Jukka Viheriälä, Mervi Koskinen, **Antti T. Aho**, and Mircea Guina, "High-power temperature-stable GaInNAs distributed Bragg reflector laser emitting at 1180 nm," Opt. Lett. 41, 657-660 (2016)

[VI] V.-M. Korpijärvi, J. Viheriälä, **A. T. Aho**, and M. Guina, "Single-mode 1180 nm GaInNAs/GaAs DBR laser diode for frequency doubling to 590 nm," in 2015 European Conference on Lasers and Electro-Optics - European Quantum Electronics Conference, (Optical Society of America, 2015), paper CB_11_4.

[VII] T. Uusitalo, H. Virtanen, J. Viheriälä, J. Salmi, **A. T. Aho**, and M. Dumitrescu, "Dual-Mode Behavior in Multi-Section DFB Semiconductor Lasers with Laterally-Coupled Ridge-Waveguide Surface Gratings," in 2015 European Conference on Lasers and Electro-Optics - European Quantum Electronics Conference, (Optical Society of America, 2015), paper CB_P_26.

[VIII] M. Dumitrescu, T. Uusitalo, H. Virtanen, J. Viheriälä, J. Salmi, and **A. T. Aho**, "Dual-Mode Multi-Section Lasers with Nanoscale Surface Gratings," in 2015 Conference on Lasers and Electro-Optics Pacific Rim, (Optical Society of America, 2015), paper 26I3_2.

[IX] Topi Uusitalo, Heikki Virtanen, Jukka Viheriälä, Joel Salmi, **Antti T. Aho** and Mihail Dumitrescu, "Difference frequency modulation of multi-section dual-mode lasers with nanoscale surface gratings", Proc. SPIE 9767, Novel In-Plane Semiconductor Lasers XV, 97670S (March 7, 2016)

LIST OF FIGURES

LIST OF TABLES

LIST OF ABBREVIATIONS AND SYMBOLS

Abbreviations and terms

AR coating Antireflection coating, a thin film structure that decreases the reflectance e.g. from a SOA facet.

COD Catastrophic optical damage, damage to a component's facets resulting from optical absorption and the resulting heating.

EAM Electro-absorption modulator, a component that can modulate the intensity of a laser beam using electrical voltage.

EDFA Erbium doped fiber amplifier.

FCC Face-centered cubic lattice structure.

FF Farfield, the profile of a laser beam far from the beam waist.

FP Fabry-Perot, e.g. Fabry-Perot laser is a simple laser consisting of two mirrors and a gain medium.

ICP Inductively coupled plasma

ILV measurement Current (I), optical power (L) and voltage (V) measurement.

LPE Liquid-phase epitaxy.

MBE Molecular beam epitaxy.

MOSFET Metal-oxide-semiconductor field-effect transistor.

OMVPE Organometallic vapor-phase epitaxy.

PECVD Plasma-enhanced chemical vapour deposition.

QW Quantum well.

RF Radio frequency.

RHEED Reflection high-energy electron diffraction.

RIE Reactive ion ethching.

RWG Ridge waveguide, a structure where a semiconductor ridge acts as a waveguide for light.

SCH Separate confinement heterostructure.

SCL Strain compensation layer.

SOA Semiconductor optical amplifier.

TW amplifier Travelling wave amplifier. An amplifier type which has negligible feedback from the component facets.

UV Ultraviolet.

VCSEL Vertical cavity surface emitting laser, a type of laser where the output of the light is on top of the component instead of on the component's edge as with edge emitting lasers.

WDM Wavelength division multiplexing. A method where several optical signals with different wavelengths are merged together.

Symbols

E_g	Band gap
B	Bimolecular recombination coefficient
q	Carrier charge
N	Carrier density
τ	Carrier lifetime
L	Cavity length
E_c	Conduction band energy level
t_c	Critical thickness
J	Current density
η_d	Differential quantum efficiency
P_{el}	Electrical power consumption
e^-	Electron

R	Facet power reflectance
ν	Frequency
g_{0N}	Gain coefficient
ν_g	Group velocity
h^+	Hole
g	Incremental gain
I	Injection current
η_{inj}	Injection efficiency
$\langle \alpha_i \rangle$	Internal losses per unit length
η_i	Internal quantum efficiency
α_m	Mirror losses
A_m	Modal area
g_m	Modal gain, Γg
w_{mode}	Mode width
A	Monomolecular recombination coefficient
V_{op}	Operating voltage
Γ	Optical confinement factor
P	Optical power
N_p	Photon density
E_p	Photon energy
τ_p	Photon lifetime
h	Planck constant
w_{RWG}	Ridge width
P_s	Saturation power
S	Slope efficiency
c	Speed of light
β_{sp}	Spontaneous emission factor
R_{sp}	Spontaneous emission rate
T	Temperature
I_{th}	Threshold current
J_{th}	Threshold current density
N_{tr}	Transparency carrier density
J_{tr}	Transparency current density
G	Total gain (output per input)
g_0	Unsaturated modal gain
E_v	Valence band energy level
V	Volume of the active region
λ	Wavelength

1. INTRODUCTION

Semiconductor optical amplifiers are optoelectronical components that are used in optical communication systems and integrated optics [8]. In optical communications they can be used for direct amplification of optical signals in various ways: as power boosters in transmitters, signal amplifiers in repeaters and preamplifiers in receivers [9]. They also have alternative uses, such as wavelength conversion [10] and all-optical logic gates [11].

The operating principle of SOAs is similar to semiconductor lasers. Optical gain is provided by stimulated emission that is enabled by the inversion of the charge carrier population in the amplifier's active region. The feature that separates SOAs from lasers is that the optical feedback - usually the reflection from the component's facets - should be as small as possible in most SOA designs. These SOAs are called travelling wave (TW) amplifiers. There is another SOA design called Fabry-Perot (FP) amplifier in which the feedback and the resulting modulation in the gain spectrum is desirable, but its usefulness in optical networks is limited. [8, 12]

The development of SOAs has followed the development of semiconductor lasers due to the similarities in the structure. First SOAs had a double heterostructure as the active region. Newer SOAs use quantum wells or quantum dots to provide the amplification since these designs provide many of the same benefits to SOA's as they do to lasers. [8, 12]

Another design strategy for SOAs is a tapered amplifier that has a horizontally widening waveguide. This has advantages such as mitigating the heating of the component due to a larger current injection area and enabling a higher output power without catastrophic optical damage (COD) due to the optical power being distributed over a larger area at the facet. The drawbacks are possible beam deterioration due to nonlinear effects such as self-focusing and filamentation. [13]

The popularity of SOAs as linear amplifiers especially in long-haul systems has de-

clined due to erbium doped fiber amplifiers (EDFAs). They often provide higher gain without the nonlinear effects of the SOAs, their noise levels are lower and their crosstalk properties better in multi-channel operation. Still, the SOA is applicable in many cases due to its cost-effectiveness and monolithic integrability with other optical components. Also the nonlinearity can be an asset in all-optical signal processing. [8]

This thesis focuses on SOAs as integrated amplifiers in an optical interconnect system. The main purpose is to support the development of an intra-system optical link for the transmission of data. In this context the primary requirements of the SOA are good integrability, sufficient amplification and as low power consumption as possible to reduce heat generation. For these reasons, a traditional, non-tapered RWG SOA has been selected to facilitate the integration and the coupling of the SOA to the rest of the system.

An example of the SOA usage in the target application is shown in figure 1.1. The source lasers have a known output power. All the interfaces and components in the system incur losses to the propagating optical signal. These losses need to be compensated by the SOA because when reaching the receiver photodiode the signal power must be sufficient for the optical link to function.
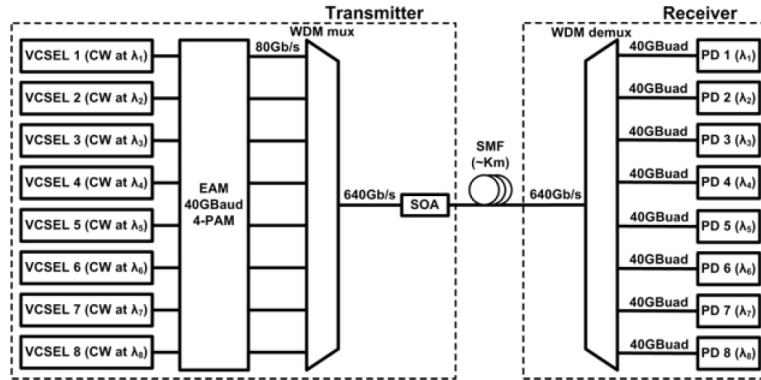
Figure 1.1 *The vertical cavity surface emitting lasers (VCSELs) on the left produce optical power in the system at different wavelengths λ_i. Their signals are modulated using electro-absorption modulators (EAM). Then the signals are combined using wavelength division multiplexing (WDM). The multiplexed signal is amplified using the SOA and then transmitted over an optical fiber to the receiving end of the system. There the different wavelengths in the signal are demuxed and fed to separate photodiodes. Adapted from [1].*

The main goal of this thesis was to develop a systematic method that can be used to determine an optimal length of a SOA. The semiconductor material and the fabrication process are not considered, but rather how to make most of an exiting design.

Two different materials are studied. The primary material is a GaInNAsSb/GaAs structure that is specifically designed for the target application with a focus in good performance even at higher temperatures. The performance of this novel material is compared to a more traditional AlGaInAs/InP structure that is similar to those used in many standard semiconductor lasers used in optical communications. [14, 15]

2. THEORY

In this chapter the used materials, the physical structure of the SOA, and its operating principles are introduced. Additionally section 2.4 covers the theory behind the core subject in this thesis, the length optimization of a SOA component.

2.1 Gallium-arsenide material system

Modern electornics and optoelectronics are based on semiconductors. Especially silicon (Si), the commercially dominating semiconductor, has established itself for use above all in transistors. Its advantages are ease of manufacturing compared to many other semiconductors, good purity, suitable mechanical properties and large wafer sizes. Additionally its surface passivation is easy using SiO_2 which is important for creating common metal-oxide-semiconductor field effect transistors (MOSFETs) [5]. A major disadvantage of silicon is that it has an indirect bandgap which greatly reduces its ability to emit light.

Semiconductors are divided into two groups based on their constituent atoms: elemental semiconductors such as Si and germanium (Ge) and compound semiconductors such as gallium arsenide (GaAs) and indium phosphide (InP). Although elemental semiconductors are easier to manufacture, compound semiconductors have distinct advantages, such as high carrier mobility, light emission cabability and bandgap engineering possibility that make them useful in optoelectronics and high-speed electronics. [5]

GaAs is called a III-V semiconductor due to gallium being an element of the third group and arsenic of the fifth group. Other notable III-V semiconductors are e.g. GaSb, GaN, AlAs and InP. In addition to these binary compounds, these elements can also be used to create ternary and quaternary compounds that have a wider range of lattice constants and bandgaps [2]. Figure 2.1 shows some examples of III-V semiconductor bandgaps and lattice constants as well as some ternary compounds

with varying compositions. In the figure, binary semiconductors are located at the marked points, ternary semiconductors along the lines connecting the points and quaternary and pentenary semiconductors in the areas limited by the points and the lines. Only the semiconductors marked as Γ-valley in the figure have a direct bandgap and are suitable for emitting light. Due to limitations caused by strain, usually only compounds in the vertical areas around substrate lattice constants are viable.
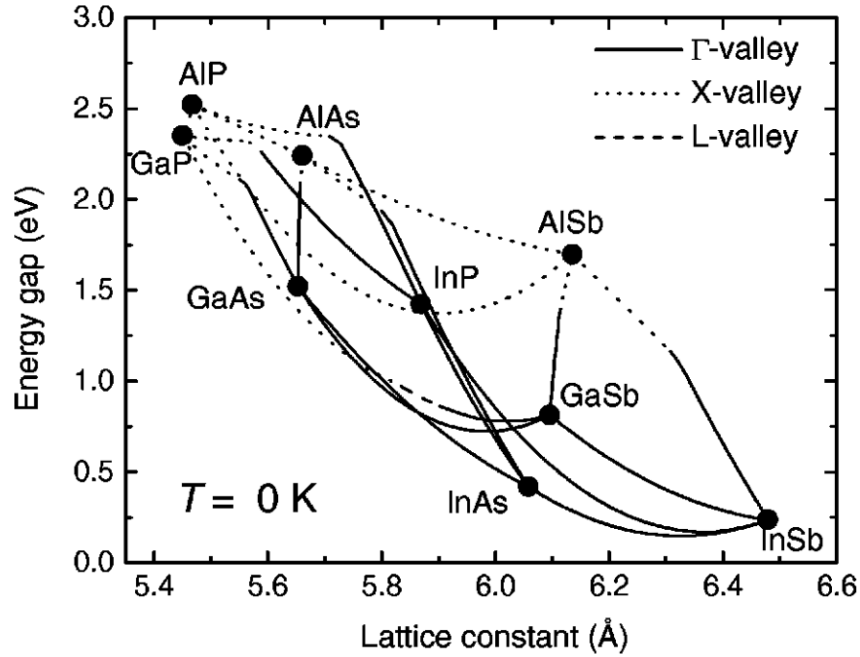
Figure 2.1 *Lattice constants and bandgaps of binary compounds and some ternary semiconductors.* [2]

2.1.1 GaAs lattice structure

GaAs has a periodic, repeating crystal structure that is called the zinc-blende lattice (see figure 2.2). Both Ga and As atoms are located at the sites of a face-centered cubic (FCC) lattice structure, and these FCC lattices are interlocked [16]. Each Ga atom is bound to four nearest As atoms and vice versa.

In ternary and quaternary semiconductors, atoms from the third group occupy the corresponding positions in the lattice as do the atoms from the fifth group. In these
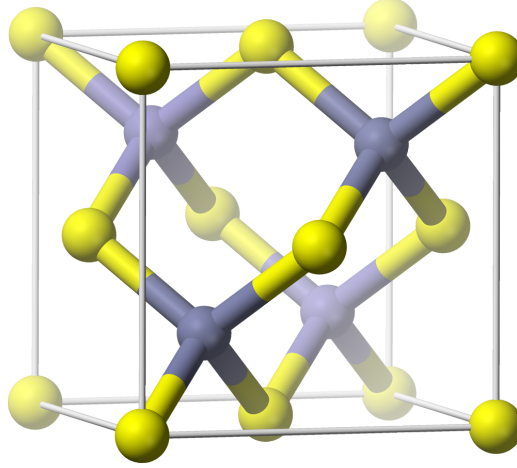
Figure 2.2 *Zinc-blende lattice structure.*

more complex semiconductors there is always the same number of III and V group atoms; the fraction of each constituent atom can be marked e.g. as $Al_xGa_{1-x}As_yP_{1-y}$ with the sums of III and V atoms' fractions both being unity.

2.1.2   Epitaxy and lattice matching

Epitaxial growth means the growing of semiconductor on top of an existing semiconductor lattice so that the grown layer has the same crystal lattice structure as the substrate. The grown layer should have a lattice constant very close to the lattice constant of the substrate. A difference in the lattice constants causes the grown layer to become either compressively or tensilely strained depending on the direction of the mismatch (see figure 2.3). If the thickness of the strained layer exceeds a critical thickness t_c, the tension is released as defects or dislocations of the lattice structure which impair the properties of the semiconductor. [3]

In some cases, such as quantum wells, a small amount of strain is desirable to improve the material properties such as gain, transparency carrier density and valence band carrier effective mass [3]. The critical thickness can be increased by using strain compensation layers (SCLs) that have an opposite lattice mismatch compared to the quantum well [17]. The most important effect of strain is that it removes the valence band energy level degeneracy of the light hole and heavy hole bands, thus reducing the density of states and making population inversion easier to achieve [16].

Methods of achieving epitaxial growth include liquid-phase epitaxy (LPE), organometal-
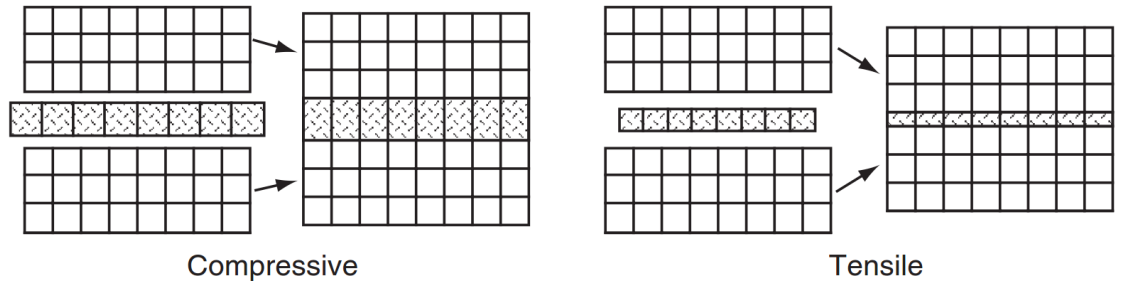
Figure 2.3 *Compressive and tensile strain in an epitaxially grown semiconductor. The lattice mismatched layer is located between two layers with equal lattice constants. [3]*

lic vapor-phase epitaxy (OMVPE) and molecular beam epitaxy (MBE) [3]. The SOAs that are analyzed in this thesis are grown using MBE which is explained in more detail in subsection 3.1.1.

2.2 Structure of the SOA
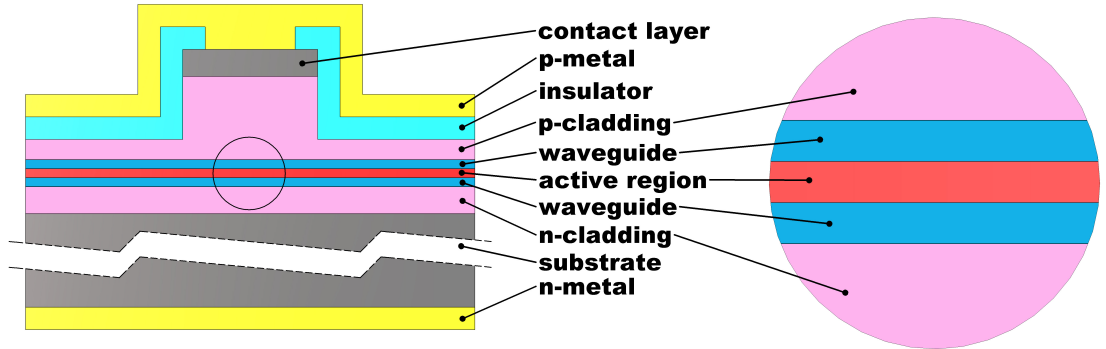
Figure 2.4 *Schematic cross section of a SOA component (not to scale). The semiconductor layer structure can be seen in the vertical direction and the surface ridge geometry in the transverse section.*

The SOA chips and RWG lasers that are analyzed in this thesis are about $100\,\mu m$ thick, $300\,\mu m$ wide and $400\,\mu m$ to $1600\,\mu m$ long. A diagram of the structure of the SOA can be seen in figure 2.4. The semiconductor layer structures of the primary and secondary materials can be seen in tables 2.1 and 2.2 respectively. In the following subsections the different layers of the SOA are reviewed from the bottom to the top.

Table   2.1 *The semiconductor layer structure of the primary material including the substrate and the epitaxially grown layers.*

Material	Thickness (nm)
p-GaAs contact	50.00
p-GaAs contact	150.00
p-AlGaAs cladding	1000.00
GaAs WG	100.00
GaNAs SCL barrier	
GaInNAsSb QW	
GaNAs SCL barrier	
GaInNAsSb QW	
GaNAs SCL barrier	
n-GaAs WG	100.00
n-AlGaAs cladding	1000.00
n-GaAs buffer	300.00
n-GaAs substrate	500×10^3

Table   2.2 *The semiconductor layer structure of the secondary material including the substrate and the epitaxially grown layers.*

Material	Thickness (nm)
p-InGaAs contact	150.00
p-InP cladding	1570.00
AlInAs carrier confinement layer	50.00
AlGaInAs WG	80.00
$Al_{0.055}Ga_{0.295}InAs$ barrier	
$Al_{0.174}Ga_{0.37}In_{0.456}As$ QW	
$Al_{0.055}Ga_{0.295}InAs$ barrier	
$Al_{0.174}Ga_{0.37}In_{0.456}As$ QW	
$Al_{0.055}Ga_{0.295}InAs$ barrier	
$Al_{0.174}Ga_{0.37}In_{0.456}As$ QW	
$Al_{0.055}Ga_{0.295}InAs$ barrier	
$Al_{0.174}Ga_{0.37}In_{0.456}As$ QW	
$Al_{0.055}Ga_{0.295}InAs$ barrier	
AlGaInAs WG	80.00
n-AlInAs carrier confinement layer	100.00
n-InP cladding	500.00
n-InP substrate	350×10^3

2.2.1   n-metal

The n-side of a SOA chip is coated with layers of different metals to improve the adhesion to the semiconductor and reduce the contact resistance. The goal is to create an Ohmic contact to the metal-semiconductor interface. The metals need a

suitable work function, electron affinity and diffusion properties, and since no single metal has the suitable properties, a combination of metals is used. Creating an Ohmic contact to compound semiconductors is more difficult compared to e.g. Si or Ge due to the metals' reactivity to the constituents of the compound. The metal combination Ni/Au/Ge/Au is often used. The roles of the different metals can be simplified as follows: [18, 5]

- Ni removes the native oxide that is formed on the surface of the n-GaAs substrate. It also diffuses into the GaAs lattice and enables the other metals to react with GaAs.

- Ge mixes with the semiconductor and adds to the n-type doping, which improves the conductivity.

- Au forms a stable Au–Ga compound with the Ga in the semiconductor.

2.2.2   Substrate

The substrate is the macro-crystal base on which the structure of the SOA has been grown and processed. The lattice constant of the substrate determines the lattice constants of the layers that can be grown on it using epitaxial growth since the lattice mismatch has to be kept small [9]. The substrate is n-doped to increase the electrical conductivity [19]. The primary material for the SOAs has a GaAs substrate and the secondary material an InP substrate.

2.2.3   Cladding, waveguide and barriers

The cladding, waveguide and barrier layers form a separate confinement heterostructure (SCH) around the quantum wells. The aim is to confine both the light and the charge carriers in the growth direction. The advantage of the SCH is that the mechanisms for light and carrier confinement are separate and can be controlled individually. The optical confinement is provided primarily by the difference in refractive indices between the cladding and the waveguide layers. The charge carriers, electrons e^- and holes h^+, are mainly confined by the potential well formed by the barrier layers with a larger band gap than the quantum wells. The waveguide and the cladding layers have a higher band gap than the barriers, but they are too thick

to effectively confine charge carriers. However, the higher band gap prevents the absorption of the photons generated in the active region making the cladding and waveguide layers transparent to the light the component emits. [3]

Figure 2.5 shows the optical field intensity distribution inside a SOA component made from the primary material with the waveguide layers and ridge geometry visible.
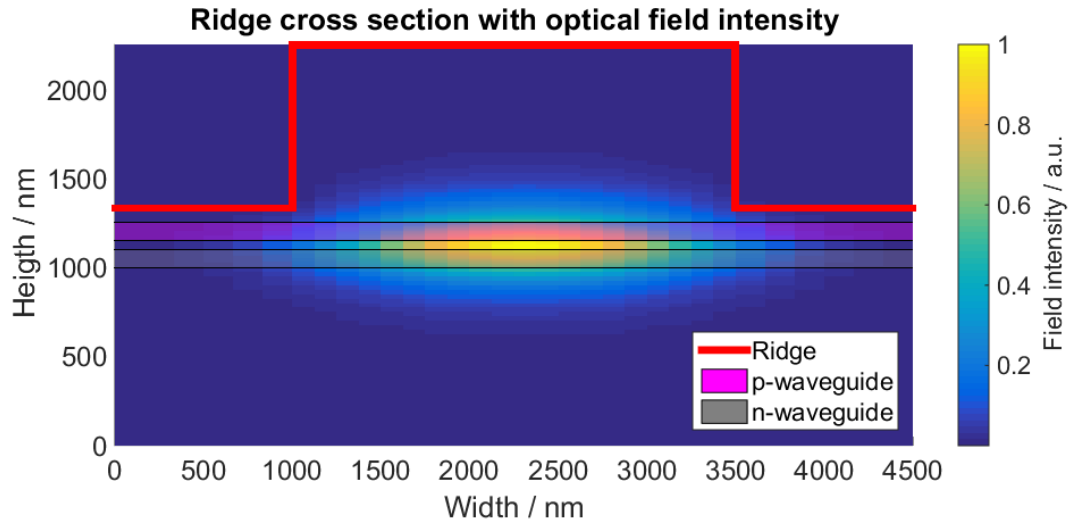
Figure   2.5 *Cross section of the optical field intensity inside the SOA made from the primary material.*

2.2.4   Active region

The active region is the part that provides the amplification for the SOA. It consists of multiple quantum well layers and barriers that are grown epitaxially. In the primary material the active region contains two quantum wells, and in the secondary material four quantum wells. In the primary material the barriers surrounding the quantum wells act also as strain compensation layers (SCLs) that allow for greater critical thickness of the lattice mismatched quantum wells without dislocations occurring [17].

2.2.5 Contact layer

A layer of p-doped semiconductor that is grown epitaxially over the p-side cladding. This layer is heavily doped to decrease the contact resistance to the p-metal as well as increase the electrical conductivity [18, 5].

2.2.6 p-metal

As with the n-side of the SOA, the p-side too is coated with layers of different metals in order to create an Ohmic contact. Contrary to the n-side, the mixing of the p-metals is undesirable. Usually the combination Ti/Pt/Au is used. Ti has a good adhesion to the semiconductor. It also acts with Pt to prevent the diffusion of Au into the semiconductor. Au is selected due to its high conductivity. [18, 5]

2.3 Optical gain and amplification

The basis to the functionality of a SOA component is optical amplification. This section provides the fundamental theory on which the design and operation of SOAs are based.

2.3.1 Semiconductor band structure

The electrons in individual atoms occupy discrete energy levels determined by quantum mechanics and Schrödinger's equation. When atoms bond together covalently and form a semiconductor lattice the uppermost energy levels in the atoms develop into two bands: the valence band and the conduction band. Both bands consist of discrete energy states but these states are so closely spaced they appear continuous. [3] The structure of the energy bands in GaAs can be seen in figure 2.6.

The valence band is the result of the degeneracy of the highest occupied atomic energy levels in the atoms forming the semiconductor. All the states in the valence band are filled in a semiconductor at $0\,\text{K}$. [3]

The conduction band forms from the first unoccupied energy level of the atoms in the semiconductor. The conduction band is empty at $0\,\text{K}$ in semiconductors. [3]
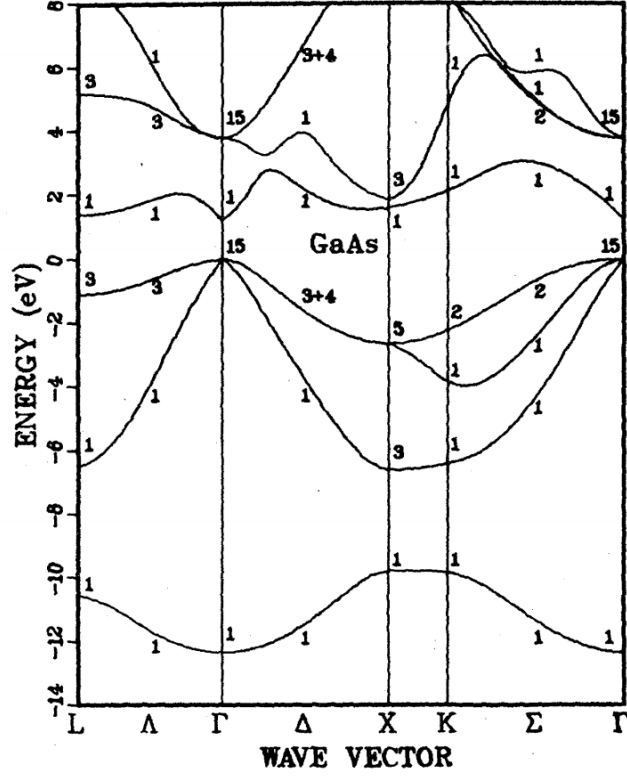
Figure 2.6 *The energy band structure of GaAs. The valence bands are at energy levels from −6 eV to 0 eV and the conduction band from 1 eV to 2 eV. [4]*

Since electrons are fermions, above zero kelvin the electron population in the valence and conduction bands follow Fermi-Dirac statistics [16].

The region between the conduction band minimum E_c and valence band maximum E_v is called the energy bandgap. In an ideal semiconductor there are no electron states in the energy bandgap, and the size of the gap $E_g = E_c - E_v$ determines the wavelength λ of emitted photons in a laser by $\lambda = hc/E_g$, where h is the Planck constant and c the speed of light. [16]

The electrons can be excited from the valence band to the conduction band by e.g. thermal energy or photons. This leaves electron vacancies in the valence band called holes. Both the holes in the valence band and the electrons in the conduction band can conduct electricity in the semiconductor. [3, 16]

2.3.2 Recombination and excitation

Electrons in the conduction band can lose energy and fill a hole in the valence band; this is called recombination. Recombination can be non-radiative (no photon is emitted) or radiative (the energy of the recombining electron is released as a photon). Similarly an electron in the valence band can absorp a photon with energy larger than or equal to the band gap and be excited to the conduction band. A diagram showing the different types of radiative recombination and absorption is shown in figure 2.7. [9]
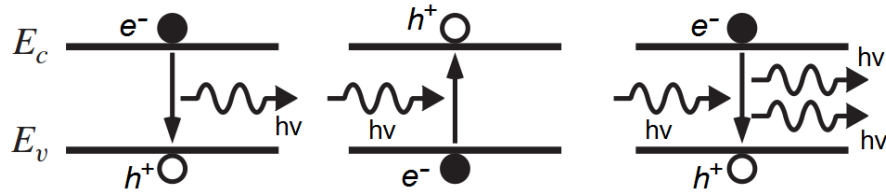
Figure 2.7 *Radiative recombination and absorption. From left to right: spontaneous emission, absorption and stimulated emission. E_c and E_v are the conduction band and valence band energy levels respectively and $h\nu$ is their difference. In spontaenous emission an electron in the conduction band recombines with a hole in the valence band and a photon is emitted. In absorption an electron in the valence band absorps a photon and is excited to the conduction band. In stimulated emission a photon causes an electron to recombine and a new photon is emitted. Adapted from [3]*

When an electron recombines non-radiatively, its energy is dissipated as phonons in the semiconductor crystal lattice. It can be caused by lattice defects, impurities in the semiconductor and the interfaces between two semiconductor layers [9]. Another important non-radiative recombination mechanism is Auger recombination in which the energy released in the recombination is transferred to another electron or hole as kinetic energy [3].

Radiative recombination can happen either as spontaneous emission or stimulated emission. The energy of the released photons $h\nu$ is the difference between the conduction band and valence band energies $h\nu = E_c - E_v$. [9]

The photons generated by spontaneous emission are incoherent and their direction is random. The light emitted by light emitting diodes (LEDs) is primarily from spontaneous emission [3]. In SOAs the spontaneous emission is a source of noise [12].

In stimulated emission an incident photon causes an excited electron to recombine radiatively, and the photon generated has the same energy, phase and direction as the original photon. This mechanism provides the gain in semiconductor lasers and SOAs. Since the probability for stimulated emission and photon absorption is the same, a population inversion is required for the stimulated emission to dominate. This means that more electrons should be in an excited state in the conduction band than relaxed in the valence band in order to enable the amplification of stimulated emission. [9]

Another requirement for effective radiative recombination is that the semiconductor must have a direct bandgap, i.e. that electrons must have the same crystal momentum at the valence band maximum and the conduction band minimum, so that crystal momentum is conserved during the recombination. This can be seen to be true for GaAs at Γ point in figure 2.6. Other direct bandgap semiconductors are e.g. InP, InAs and GaSb as well as many ternary and quaternary semiconductors such as AlGaAs and InGaAs. Examples of indirect bandgap semiconductors are Si and Ge. In semiconductors with an indirect bandgap radiative recombination requires interaction with the phonons in the lattice which greatly reduces the probability of radiative recombination. [3, 9]

2.3.3 Quantum well and barrier layers

In bulk semiconductor the energy states in the conduction and valence bands are so closely spaced they appear continuous and electrons and holes are free to move in the three dimensional lattice in the conduction and valence bands respectively. To improve the recombination efficiency of the active region the electrons and holes can be trapped near each other using a quantum well (QW) structure. [3]

The QW consists of a thin layer of a semiconductor sandwiched between barrier layers with a higher bandgap. There are different types of QWs depending on the alignment of the conduction and valence bands. The band gap in the type I QW is smaller than in the surrounding semiconductor, and both the electrons and holes become trapped in a potential well. Typical thicknesses for QWs are in the order of about ten nanometers. These dimensions are so small that the available energy states are quantized. Since the quantized energy levels are above the conduction band minimum energy and below the valence band maximum energy, the quantization increases the energy of the photons emitted when electrons recombine

radiatively from the lowest conduction band energy level to the highest valence band energy level. This recombination energy E_1 can be seen in figure 2.8 as well as the general structure of the QW. Because the quantization energy depends on the potential barriers and on the QW thickness, the stimulated emission wavelength can be adjusted by adjusting the composition of the QWs and the barrier layers as well as by changing the QW thickness. [3, 16]

At high temperatures electrons and holes may gain enough thermal energy to escape the potential well in the QW. This leakage current decreases the internal quantum efficiency η_i of lasers and SOAs. [3]
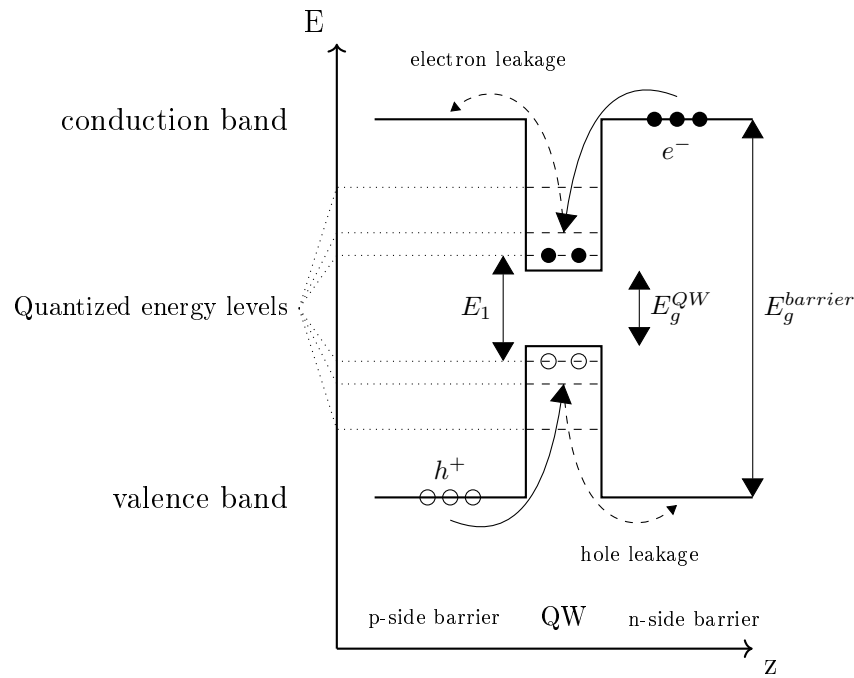
Figure 2.8 *Band structure in the quantum well and barrier layers. z is the direction perpendicular to the plane of the wafer. E_g are the band gaps for the QW and the barrier layers. E_1 is the recombination energy when an electron relaxes.*

2.3.4 Gain relations

Incremental gain g measures how much much light is amplified due to stimulated emission per unit distance when travelling in the waveguide of a laser or SOA.

Disregarding saturation, the amplification is exponential and can be modelled as

$$N_p(z) = N_p(0)e^{gz}, \tag{2.1}$$

where N_p is the density of photons and z is the distance travelled along the waveguide. [3]

The photon density and carrier density N are connected by the rate equations

$$\frac{\mathrm{d}N}{\mathrm{d}t} = \frac{\eta_{inj}I}{qV} - \frac{N}{\tau} - \nu_g g N_p \tag{2.2}$$

$$\frac{\mathrm{d}N_p}{\mathrm{d}t} = \Gamma \nu_g g N_p + \Gamma \beta_{sp} R_{sp} - \frac{N_p}{\tau_p}, \tag{2.3}$$

where η_{inj} is the injection efficiency (the fraction of the injected current that generates carriers in the active region), I the injection current, q the carrier charge, V the volume of the active region, τ the carrier lifetime, ν_g the group velocity of the light, Γ the optical confinement factor in the QW region, β_{sp} the spontaneous emission factor (the percentage of the total spontaneous emission coupled into the lasing mode), R_{sp} the number of photons generated by spontaneous emission per unit time per unit volume and τ_p the photon lifetime. [3]

2.4 Calculating the length with minimum power consumption

Many different SOA cavity lengths can be used in order to meet the target total amplification, but components with different lengths have a varying power consumption. In this chapter the steps to find the power consumption as a function of device length are introduced.

The amplification of the light along the SOA can be modelled with the differential equation

$$\frac{\mathrm{d}P(z)}{\mathrm{d}z} = \left[\frac{\Gamma \frac{\mathrm{d}g}{\mathrm{d}N} \left(\frac{\eta_{inj}I\tau}{qV_{act}} - N_{tr} \right)}{1 + \frac{P(z)}{P_s}} - \alpha_i \right] P(z) = \left[\frac{\Gamma \frac{\mathrm{d}g}{\mathrm{d}N} \left(\frac{\eta_{inj}J\tau}{qn_{QW}d_{QW}} - N_{tr} \right)}{1 + \frac{P(z)}{P_s}} - \alpha_i \right] P(z) \tag{2.4}$$

where Γ is the optical confinement factor in the QW region, $\mathrm{d}g/\mathrm{d}N$ the differential gain, η_{inj} the injection efficiency, I the injection current, J the injection current density , τ the carrier lifetime, q the carrier charge, V_{act} the active region volume,

n_{QW} the number of quantum wells, d_{QW} the thickness of a QW, N_{tr} the transparency carrier density, α_i the internal losses per unit length and P_s the saturation power. This can be simplified as [20]

$$\frac{\mathrm{d}P(z)}{\mathrm{d}z} = \left(\frac{g_0}{1 + \frac{P(z)}{P_s}} - \alpha_i \right) P(z), \qquad (2.5)$$

where g_0 is the unsaturated modal gain.

The saturation power P_s is the power level above which the gain saturation due to carrier density reduction becomes significant.

Additionally the dependence of the operating voltage $V_{op}(J)$ on the current density J needs to be known in order to be able to calculate the electrical power consumption

$$P_{el} = J L w_{RWG} V_{op}(J), \qquad (2.6)$$

where L is the cavity length and w_{RWG} the ridge width.

2.4.1 Modal gain as a function of current density

To find the dependence of the modal gain on the current density $g_m(J)$ RWG lasers with different cavity lengths L were characterized. These lasers are made from the same material as the SOAs and have the same geometry, so it is expected that their modal gain behaviour with respect to the current density is the same. From these lasers the threshold currents I_{th} and slopes S were characterized by performing ILV measurements.

Using the slopes the differential quantum efficiencies η_d can be calculated using [3]

$$\eta_d = \left[\frac{q}{h\nu} \right] \frac{\mathrm{d}P_0}{\mathrm{d}I} = \left[\frac{q}{h\nu} \right] S. \qquad (2.7)$$

These can be used to calculate the internal quantum efficiency η_i and the internal losses $\langle \alpha_i \rangle$ using the equation [3]

$$\frac{1}{\eta_d} = \frac{\langle \alpha_i \rangle}{\eta_i \ln(1/\sqrt{R_1 R_2})} L + \frac{1}{\eta_i} \qquad (2.8)$$

by fitting a line $y = kx + b$ to the component lengths L and the inverses of the differential quantum efficiencies $\frac{1}{\eta_d}$ using the least squares method. An example of such a fit is shown in figure 2.9. Then the internal quantum efficiency and the internal losses can be calculated

$$\eta_i = \frac{1}{b}$$
$$\langle \alpha_i \rangle = k\eta_i \ln(1/\sqrt{R_1 R_2}),$$

where R_1 and R_2 are the known facet reflectances.
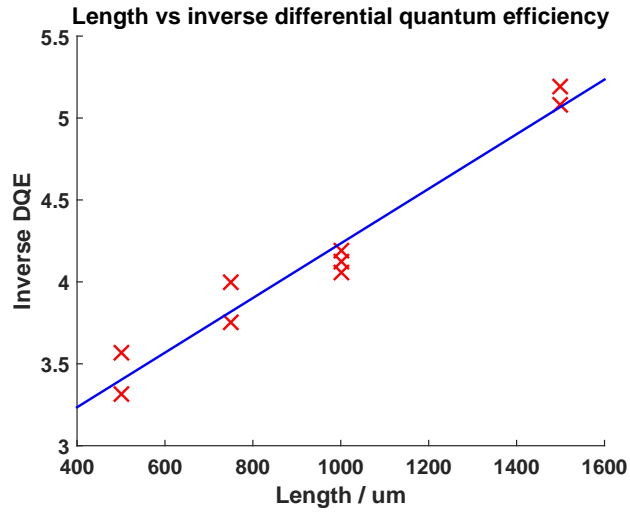
Figure 2.9 *Example fit of inverse differential quantum efficiency vs length. The data is measured from uncoated components fabricated from the primary material.*

At the laser threshold the modal gain, internal losses and mirror losses are connected [3]:

$$g_m = \langle \alpha_i \rangle + \alpha_m \tag{2.9}$$

where g_m is the modal gain and α_m is the mirror losses. The modal gain is the convolution of the transverse material gain distribution with the optical field intensity distribution which, under the assumption of a constant material gain g in the QW region, can be approximated with $g_m = \Gamma g$ where Γ is the optical confinement factor. The mirror losses for a Fabry-Perot cavity can be calculated from the facet

power reflectances R_1 and R_2 by [3]

$$\alpha_m = \frac{1}{L} \ln\left(\frac{1}{\sqrt{R_1 R_2}}\right). \tag{2.10}$$

Thus, having obtained $\langle \alpha_i \rangle$ from the RWG characterization and calculated the mirror losses using known facet reflectances and cavity lengths, the threshold modal gains for the different cavity lengths $g_m(L)$ were obtained. Also the threshold current densities $J_{th}(L)$ for these cavity lengths could be calculated from the threshold currents I_{th} using

$$J_{th} = \frac{I_{th}}{L w_{RWG}}. \tag{2.11}$$

Combining $g_m(L)$ and $J_{th}(L)$ the dependence of the threshold modal gain on the threshold current density $g_m(J_{th})$ can be obtained.

It is approximated for the SOAs that the transverse optical field distribution, the carrier density and the modal gain are constant in the longitudinal direction along the SOA. This approximation should be valid when the SOA is operated under the saturation power P_s. With this approximation the SOA components are expected to have a similar modal gain dependence on the current density as the characterized RWG lasers, and the modal gain – current density relationship $g_m(J)$ is obtained for the SOA components in the current density range determined by the threshold current densities of the available laser components.

The g_m–N relationship of an ideal component can be expressed as [3]

$$g_m = g_{0N} \ln \frac{N}{N_{tr}}, \tag{2.12}$$

where g_{0N} is a gain coefficient and N_{tr} is the transparency carrier density. This can be presented using current densities instead of carrier densities with the help of equation 2.16:

$$g = g_{0N} \ln \frac{\tau(J)J}{\tau(J_{tr})J_{tr}}, \tag{2.13}$$

where τ is the carrier lifetime as a function of the current density and J_{tr} is the transparency current density. The equation 2.13 can be used to extrapolate the values of the modal gain at higher current densities than those that can be achieved with the threshold currents of the characterized RWG components.

2.4.2 Calculation of carrier lifetime dependence on current density

At and below the lasing threshold (with $N_p \approx 0$) and under steady-state conditions (with $\frac{\mathrm{d}N}{\mathrm{d}t} \approx 0$) equation 2.2 can be modified to

$$\frac{N}{\tau} = \frac{\eta_{inj} I}{qV} \tag{2.14}$$

$$\frac{N}{\tau} = \frac{\eta_{inj} J}{qd} \tag{2.15}$$

$$N = \frac{\eta_{inj}\tau}{qd} J \tag{2.16}$$

and $\mathrm{d}N$ can be expressed as

$$\mathrm{d}N = \frac{\eta_{inj}\tau}{qd}\,\mathrm{d}J \tag{2.17}$$

and thus differential gain may be written as

$$\frac{\mathrm{d}g}{\mathrm{d}N} = \frac{qd}{\eta_{inj}\tau}\frac{\mathrm{d}g}{\mathrm{d}J}. \tag{2.18}$$

With this result, the obtained g_m–J relationship can be used to calculate the differential gain at different current densities.

The carrier lifetime also depends on the carrier concentration and through that the current density [3]:

$$\tau = \frac{1}{A + BN_{th} + CN_{th}^2} \tag{2.19}$$

$$\tau = \frac{1}{A + B(\frac{\eta_{inj}\tau}{qd}J) + C(\frac{\eta_{inj}\tau}{qd}J)^2} \tag{2.20}$$

$$\tau = \begin{cases} T(J) \\ T_+(J) \\ T_-(J) \end{cases} \tag{2.21}$$

where A is the monomolecular recombination coefficient, B is the bimolecular recombination coefficient and C is the Auger recombination coefficient. This equation has three solutions only one of which, $T(J)$, has non-complex and non-negative values with reasonable values for the parameters. For this reason $T(J)$ is chosen to represent the carrier lifetime as a function of injection current density. The explicit forms of the solutions are presented in Appendix A.

The values of the constants A, B and C for the primary material are approximated by the reported values for GaInNAs quantum wells with 36% In-content and 1.7% N-content at 300 K [21]. The values are presented in Table 4.1. The carrier lifetime of the primary material is presented in Figure 2.10.
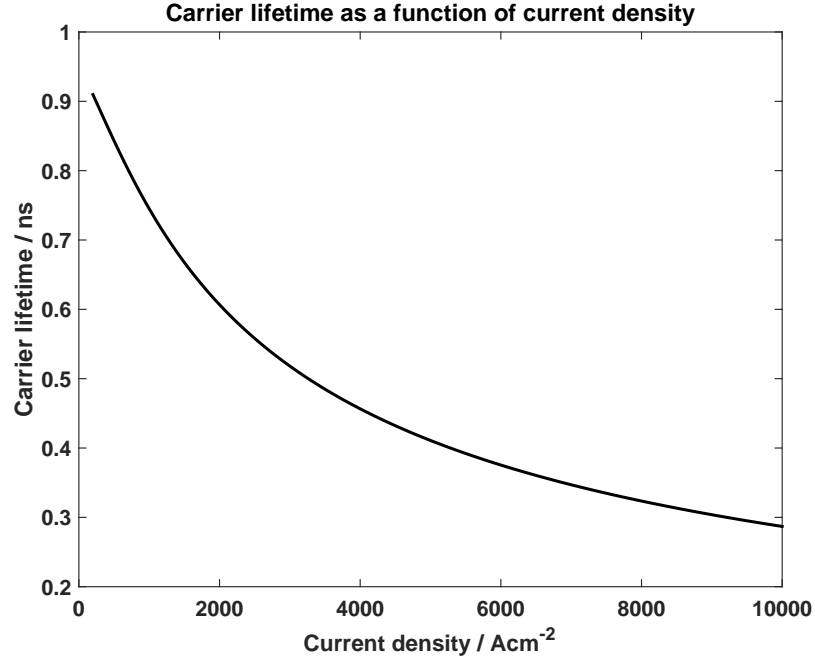
Figure 2.10 *Carrier lifetime for the primary material as a function of injection current density.*

2.4.3 Operating voltage as a function of current density

The dependence of the operating voltage V_{op} on the current density is also needed so that the power consumption at a certain injection current can be calculated. For this, the same ILV data that was used in obtaining the modal gain can be used.

The operating voltage is expected to depend on the injection current density and components with different lengths but the same ridge widths are expected to have the same operating voltage when they are operated at the same current density.

The current–voltage relationship of the IV measurements is transformed into J–V relationship using known component ridge widths and lengths. This way the IV data

from all the components can be used to construct an interpolating function $V_i(J)$ that can be used to get the operating voltage at certain injection current density. It was determined empirically that a function of the form

$$V_i(J) = (c_1 \ln(J)^{c_2} + c_3 J)^{c_4}, \tag{2.22}$$

where c_1, c_2, c_3 and c_4 are fitting parameters, fits the J–V data well.

2.4.4 Calculation of the device length providing the target output optical power

The SOA length L_{req} that provides the target output optical power for a given input optical power and a fixed injection current density is calculated using equation 2.5.

The SOA saturation power from equation 2.5 is given by [22]:

$$P_s = \frac{h\nu A_m}{\tau \frac{\mathrm{d}g}{\mathrm{d}N}} = \frac{h\nu n_{QW} d_{QW} w}{\Gamma \tau \frac{\mathrm{d}g}{\mathrm{d}N}}, \tag{2.23}$$

where ν is the photon frequency and A_m the modal area in the approximation of uniform transverse optical field intensity:

$$A_m \Psi_{max}^2 = \iint_{\pm\infty} \Psi^2 \,\mathrm{d}x\,\mathrm{d}y \tag{2.24}$$

$$(n_{QW} d_{QW} w_{\Psi_{max}}) \Psi_{max}^2 = \iint_{act\text{-}reg} \Psi^2 \,\mathrm{d}x\,\mathrm{d}y \tag{2.25}$$

$$A_m \approx (n_{QW} d_{QW} w_{\Psi_{max}})/\Gamma, \tag{2.26}$$

where $w_{\Psi_{max}} = w$ is the equivalent width of the optical mode for an uniform maximum optical field intensity.

The longitudinal operation parameters (optical confinement factor in the QW area Γ, carrier density N, carrier lifetime τ and differential gain $\mathrm{d}g/\mathrm{d}N$) are assumed to be constant and close to the threshold values. With these approximations, equation 2.5 is used to calculate the SOA length L_{req} at which the target optical output power is reached for a given input optical power and injection current density.

2.4.5 Calculating the power consumption at a given injection current density and the corresponding SOA length that provides the target output optical power

Once the device length that provides the target output optical power for a given input optical power and a given injection current density is established using equation 2.5, the power consumption is calculated from the value of the injected current and the corresponding operating voltage. Thus it is possible to calculate the power consumption of SOA components that achieve the target output power with different injection current densities and device lengths.

The range of the injection current densities that can be used in the calculation is limited by the method of finding the g_m−J relationship, i.e. the threshold current densities of the measured RWG lasers. A sampling of current densities J_i can be created from the smallest observed current density J_{min} to the largest observed current density J_{max}. At each sampling point the SOA cavity length $L_{req}(J_i)$ required for target amplification is found by integrating the equation 2.5:

$$P_{out} = P(L_{req}) = GP_{in} = GP(0) = \int_0^{L_{req}(J_i)} \left(\frac{g_0(J_i)}{1 + \frac{P(z)}{P_s(J_i)}} - \alpha_i \right) P(z)\, \mathrm{d}z + P_{in}.$$

$$(2.27)$$

In practice this was done numerically using the forward finite difference method by iterating incrementally the expression

$$P(z + \Delta z) = \left(\frac{g_0(J_i)}{1 + \frac{P(z)}{P_s(J_i)}} - \alpha_i \right) P(z)\Delta z + P(z) \qquad (2.28)$$

with a small value of Δz from $z = 0$ with $P(0) = P_{in}$ until the target power was achieved.

Having found L_{req} for each applicable value of the current density J_i the power consumption as a function of the device length $P_{el}(L)$ can be calculated using equation 2.6. If our original threshold current and modal gain data covers broad enough range of values, there should be some device length $L_{optimal}$ where the power consumption $P_{el}(L_{optimal})$ is at a minimum.

3.   SAMPLES, MEASUREMENT PROCEDURE AND DATA PROCESSING

This chapter covers the practical steps of fabricating the RWG components involved in this thesis and measuring their characteristics. Section3.1 covers the fabrication steps and methods: MBE, wafer processing, dicing, packaging and antireflection (AR) coating. Section3.2 explains the different characterization methods: ILV, spectral and far field measurement. Section3.3 details the sample variants that were measured to obtain the data that is used in the analysis.

3.1   RWG laser fabrication

The fabrication of RWG lasers consists of three major process phases: epitaxial growth, wafer processing, and dicing, packaging and AR coating.

3.1.1   Molecular beam epitaxy

Molecular beam epitaxy (MBE) is an epitaxial growth method used to grow thin semiconductor layers on a substrate that in this case is an n-GaAs wafer. The growth takes place in an ultrahigh vacuum. Desired atoms are evaporated from effusion cells, and beams of these atoms condense on the substrate forming layers that have the same lattice structure as the substrate. A schematic drawing of a MBE chamber is presented in figure 3.1. [23, 3]

During MBE growth the substrate is heated to achieve proper stoichiometry between group III and group V atoms. At suitable temperature the substrate is cool enough to allow group III atoms to condense on its surface but hot enough that group V atoms evaporate unless they can form a compound with condensed group III atoms. Usual temperatures for growth vary from 600 °C to 700 °C. [3] The increased
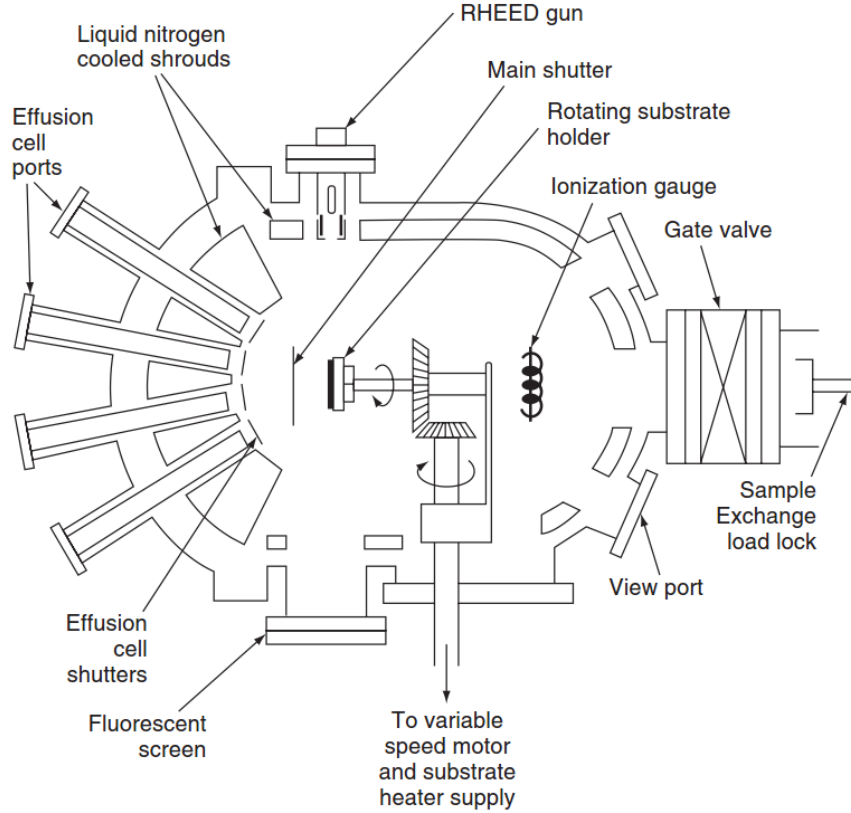
Figure 3.1 Schematic drawing of a MBE chamber. [3]

temperature is also required to give the atoms sufficient thermal energy to move to the correct positions on the lattice surface. [23] The walls of the chamber are lined with panels cooled by liquid nitrogen to condense stray atoms. [3]

The growth rate on the substrate can be monitored in real time using e.g. reflection high-energy electron diffraction (RHEED). This increases the accuracy of the layer thicknesses grown. [3]

The MBE-grown layer structure of the primary material analyzed in this thesis is described in table 2.1.

3.1.2   Wafer processing

After MBE growth the semiconductor wafer undergoes many cleanroom processing steps so that functional components can be fabricated. This subsection introduces the used processing techniques and the process sequence.

Plasma-enhanced chemical vapour deposition (PECVD)

PECVD is a deposition technique that can be used to grow thin dielectric films on a wafer. Two planar electrodes inside a vacuum chamber have a rapidly oscillating voltage between them. The sample is placed on the bottom electrode that is connected to a radio frequency (RF) generator and the top electrode is grounded. A schematic picture of a PECVD chamber is presented in figure 3.2. [5, 6]
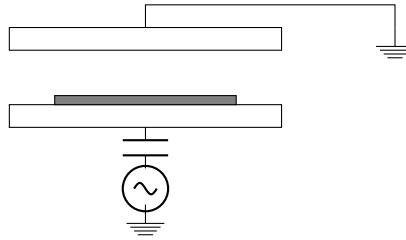
Figure 3.2 *Schematic picture of a PECVD chamber. Wafer (coloured with gray) is placed between two electrodes.*

Suitable process gasses depending on the desired film to be grown are led into the chamber, and the rapidly oscillating electric field between the electrodes dissociates the gasses into plasma. PECVD produces low-density plasma where only a small fraction of the gasses are dissociated. The plasma contains reactive radicals that stick to the wafer's surface forming a film. [5]

The growth rate and film quality have a strong dependence on the growth temperature in PECVD. [5] For the samples analysed in the thesis the growth temperature was 300°C, and grown films were SiO_2.

Reactive ion etching (RIE)

RIE is a dry-etching technique that closely resembles PECVD. The chamber layout is similar, but the difference is that in RIE the ions and neutral molecules striking the wafer do not stick but instead etch the surface.

As with the PECVD chamber, the walls of the chamber and the top electrode are grounded so no charge accumulates to them. The bottom electrode is connected to a RF generator through a capacitor, so that it gains a negative charge from the free electrons in the generated plasma. The plasma itself gains a positive charge due to electron deficiency, so there is a net voltage difference between the plasma and the bottom electrode in addition to the oscillating voltage from the RF generator. While electrons have a high mobility and can respond to the oscillating signal from the RF generator, ions are much larger and only react to the average voltage difference between the lower electrode and the plasma. The ions gain kinetic energy from the voltage difference and etch the wafer both mechanically by striking it and chemically by forming volatile compounds with the surface of the wafer. [5]

The advantage of RIE is that the etching result is ansisotropic. Since the ions strike the wafer mainly in the vertical direction, the sample is etched only little in the horizontal direction, which enables the etching of surface structures with high aspect ratios. The balance between chemical etching by the radicals in the plasma and mechanical etching by ion bombardment can be changed by changing the pressure. At high pressures there are more radicals that can react with the wafer, and also ion bombardment energy is lower due to ions colliding with gas particles. At low pressures there are fewer radicals and ions hit the wafer with higher energy. Between the two modes of etching the mechanical ion bombardment is more anisotropic but can cause damage to the surface of the wafer. [5]

One important aspect of choosing process gasses is the selectivity of the etching. Especially when using an etching mask to etch a specific pattern on the wafer it is desirable that only the wafer visible under the etching mask is etched and not the mask itself. With the process gasses selected properly, the reactive radicals in the plasma can form volatile compounds on the wafer surface that are then detached by the ion bombardment while the corrosion of the mask is minimal. [5, 6]

In the processing of the samples that this thesis is concerned with, RIE was used for the etching of SiO_2.

Inductive coupled plasma reactive ion etching (ICP)

Inductive coupled plasma reactive ion etching (ICP-RIE or ICP) is a dry etching technique that provides high density plasma that enables faster etch rates and more

control over the etching profile than RIE. [5]

A problem with RIE is that the same RF generator is used to both generate the plasma and the bias voltage for bombarding the wafer surface with ions. At high RF powers more plasma is generated but the bombardment energy also increases which may damage the wafer surface. In ICP this issue is solved by having separate power sources for plasma generation and bias voltage. A schematic of an ICP chamber is shown in figure 3.3. [5]
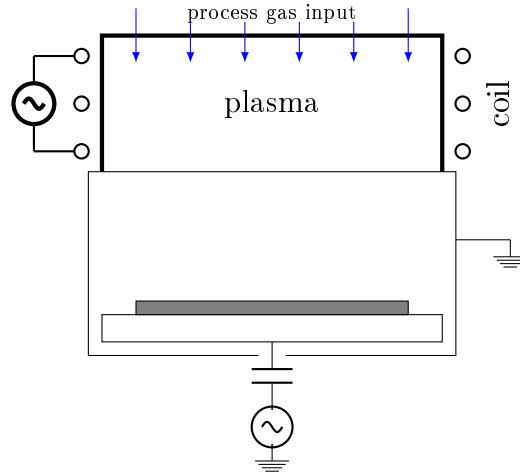
Figure 3.3 *Schematic of an ICP chamber. Plasma is generated in the upper part of the chamber. Lower part of the chamber is similar to RIE chamber with an RF-coupled electrode. Adapted from [5]*

In ICP another RF generator is connected to a coil surrounding the chamber and the changing magnetic field inside the coil generates the plasma. Since the power of the secondary RF generator doesn't affect the ion bombardment energy, much higher density plasma can be produced than in regular RIE. This in turn produces more reactive radicals and high etching speeds can be achieved even with low bombardment energies. [5]

In the processing of the samples that this thesis is concerned with, ICP was used for the etching of GaAs and AlGaAs layers to create the RWG geometry.

UV-lithography

Ultraviolet (UV) lithography is a method of patterning surfaces. Its principle is that the sample is covered with a photosensitive chemical (photoresist), a transparent screen with the desired opaque patterning is placed over the sample and then UV light is shone over the screen. Thus only the parts of the wafer under the transparent sections of the screen are exposed to the radiation, and the chemical at those locations reacts to the light.

There are different kinds of photoresists that react differently to exposure. Positive photoresists become soluble to the corresponding developer solution where exposed, and are insoluble unexposed. Negative photoresists are vice versa: without exposure they are soluble and insoluble after exposure. [6]

A third type of resist is the image reversal resist. After the first exposure it behaves like a positive photoresist but after a bake (heating to a specified temperature for a specified time) following the first exposure the exposed area becomes permanently insoluble to the developer agent. When the wafer is subsequently flood exposed (exposure without the mask), only the resist exposed before the bake remains after development. The advantage of this is the opposite wall profile of the resist which is helpful e.g. for metal lift-off processes. [6, 24]

The photoresists are applied on the wafer using spin coating: The wafer is rotated at high speed and a small amount of the resist is dropped on it. Depending on the viscosity of the resist and the rotational speed of the wafer, a layer of the resist with constant thickness remains on the wafer.

The wavelength of the UV light used for exposure imposes limits on the resolution of the features that can be fabricated. The minimum resolvable feature size is

$$l_{min} = \sqrt{\lambda h'}, \tag{3.1}$$

where λ is the wavelength of the light used and h' the distance between the wafer and the aperture which is in this case the photolithography mask, so the distance is determined by the thickness of the photoresist. This limit comes from Fresnel diffraction. [6] The minimum feature size of the mask used in the process was $2\,\mu m$ which is well above $l_{min} = 854\,nm$ with resist thickness $1.8\,\mu m$ [25] and wavelength

405 nm (mask aligner's mercury lamp's H-line emission wavelength).

In the samples studied in this thesis, all the features on the wafer (RWG, dielectric opening and metal patterns) are produced using UV-lithography. The resist patterns produced by the lithography are used as etching masks for RIE and ICP as well as for lift-off in metallization. A part of the RWG etching mask is shown in figure 3.4.
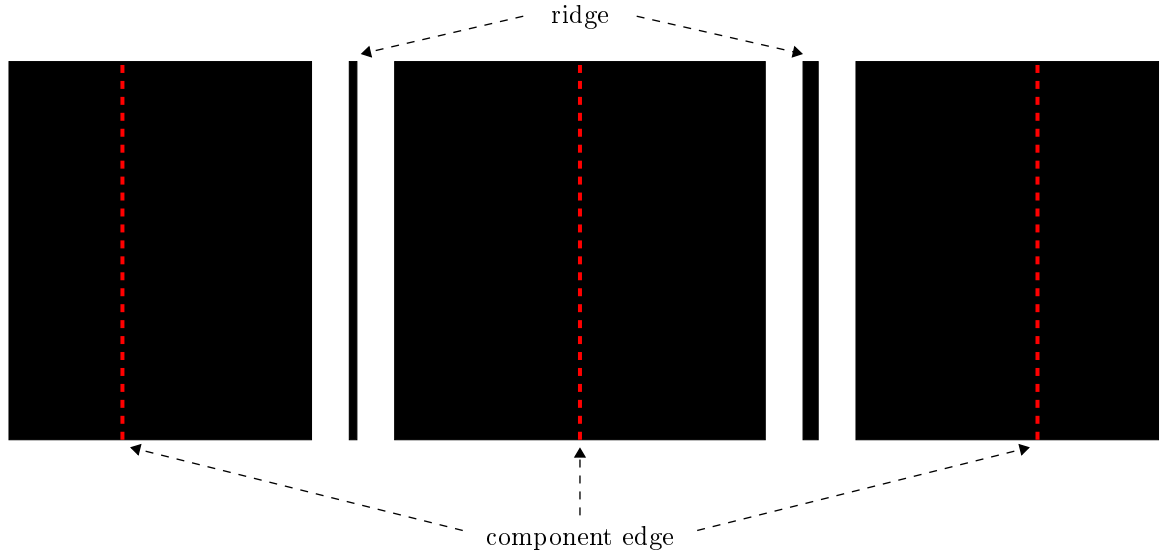
Figure 3.4 *Part of an RWG etching mask with annotations. The ridges of two neighbouring components are shown. Opaque areas are colored in black and transparent areas are white. In the photolithography the resist under the mask is exposed on the both sides of the ridges, and these areas are then etched to form the RWG structure.*

Metallization and lift-off

In the fabrication process both sides of the wafer are coated with metal (see section2.2). The metallization is done using an electron beam coating system. The wafer is placed face-down in a vacuum chamber, and desired metals are evaporated on the wafer using an electron beam. A schematic of the coating chamber is shown in figure 3.5.

The primary reasons why the evaporation has to be done in a vacuum environment with pressure below 10^{-6} Torr are that the vapor particles can travel freely from the crucible to the wafer surface and that the evaporating material doesn't react with
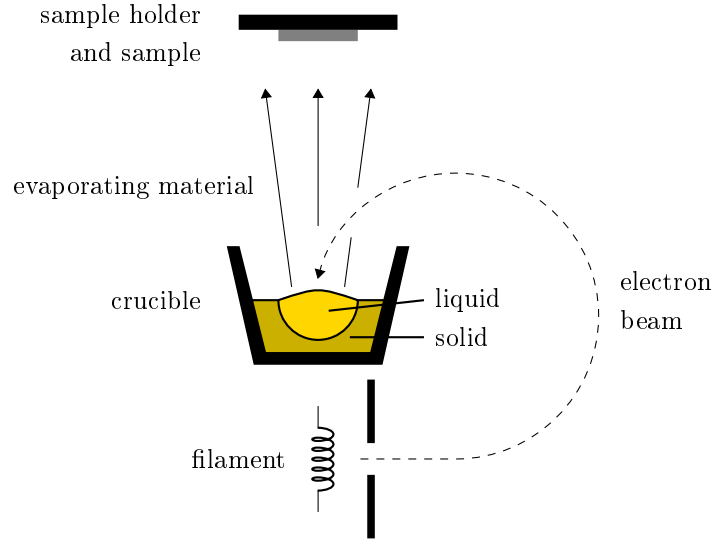
Figure 3.5 *Schematic of the e-beam metallization system. Electrons from a filament are accellerated by an electric field and a magnetic field bends the electron beam towards the source material deposited in a crucible. Part of the source material melts and is evaporated towards the sample. [6, 7]*

air and form oxides. [6, 7]

The film growth rate and thickness are monitored during evaporation using a quartz crystal placed in the chamber. The oscillation frequency of the crystal changes when the metal layer grows on it, and when the mechanical properties of the metal are known, the thickness of the layer can be calculated from the change in the oscillation frequency.

Lift-off is a procedure to form patterns in the metal layer without the need for etching. The principle is that photolithography is used to pattern the wafer with photoresist so that the areas where the deposited metal is to be located are left bare. Then the whole wafer is coated with metal, and afterwards the photoresist is dissolved removing the excess metal in the process. The exposure and resist development in the photolithography phase should be adjusted so that the walls of the resist layer have a negative slope which makes the lift-off easier. A step-by-step depiction of lift-off is shown in figure 3.6. [7]
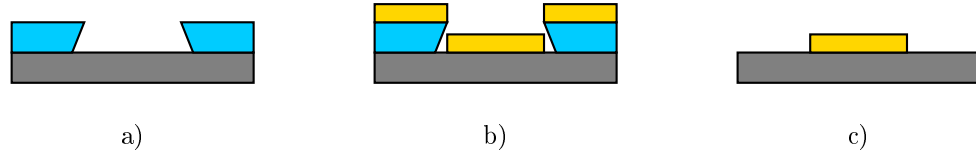
Figure 3.6 *Lift-off steps a) Photolithography using a negative or image reversal photoresist. b) Metallization of the whole wafer. Negative sloped walls of the resist prevent the metal on the wafer and the metal on the resist from becoming connected. c) Dissolution of the resist. The excess metal is removed along with the resist.*

Thinning

During processing the GaAs wafers have to be several hundreds of micrometers thick to have enough mechanical strength to survive handling [26]. However, GaAs's thermal conductivity, around $0.55 \, \text{W cm}^{-1} \, {}^\circ\text{C}^{-1}$ at room temperature [27], is quite poor compared to e.g. silicon's thermal conductivity $1.3 \, \text{W cm}^{-1} \, {}^\circ\text{C}^{-1}$ at room temperature [28]. Thick wafer also means higher electrical resistance when the components are operated. To improve the thermal and electrical performance of the components, the wafer is thinned to around $100 \, \mu\text{m}$ to $150 \, \mu\text{m}$ after most of the processing steps have been performed.

The thinning is done using a lapping device. The wafer is attached with wax to a lapping jig which presses the wafer against a lapping plate with a constant pressure. The lapping plate grinds against the wafer in the presense of an abrasive liquid containing alumina particles and the wafer is eroded. The thinning speed can be controlled by using abrasive liquids with different size alumina particles or by changing the jig pressure.

Process sequence

The main phases of the process sequence after the epitaxial growth are descibed here. Details such as sample cleaning and resist baking are omitted.

1. Growing of a SiO_2 film on the wafer and spin-coating with a positive photoresist (figure 3.7 b). The resist will be used to etch the dielectric layer, and the SiO2 layer is consequently used as an etching mask for the RWG etching step.

2. Photolithography using the RWG photolithography mask (figure 3.7 c).

3. Development of the resist (figure 3.7 d).

4. Etching of the SiO_2 layer with RIE using the photoresist as the etching mask (figure 3.7 e).

5. Removing the resist and etching of the wafer with ICP using the dielectric layer as the etching mask (figure 3.7 f).

6. Removing the remaining SiO_2 with RIE, depositing a new layer of SiO_2 and spin-coating a layer of positive photoresist (figure 3.8 g). The new layer of SiO_2 works as the insulator that makes the electrical current during component operation only flow through the RWG.

7. Photolithography using the opening photolithography mask (figure 3.8 h).

8. Development of the resist (figure 3.8 i).

9. Etching of the SiO_2 layer with RIE using the photoresist as the etching mask (figure 3.8 j).

10. Resist spinning, photolithography with the metal lift-off mask, p-side metallization and lift-off process (figure 3.8 k).

11. Wafer thinning and n-side metallization (figure 3.8 l).

After these process steps, the structure of the components is complete and the wafer is ready for dicing.

3.1.3   Dicing, packaging and antireflection coating

After the wafer processing steps the sample and subsequently separate chips undergo dicing, packaging and in some cases antireflection (AR) coating.

Dicing

Dicing is the separation of individual components from the wafer. During wafer processing, all the components are fabricated monotlithically on the same semiconductor wafer. In order to produce functional devices, the wafer needs to be first cut
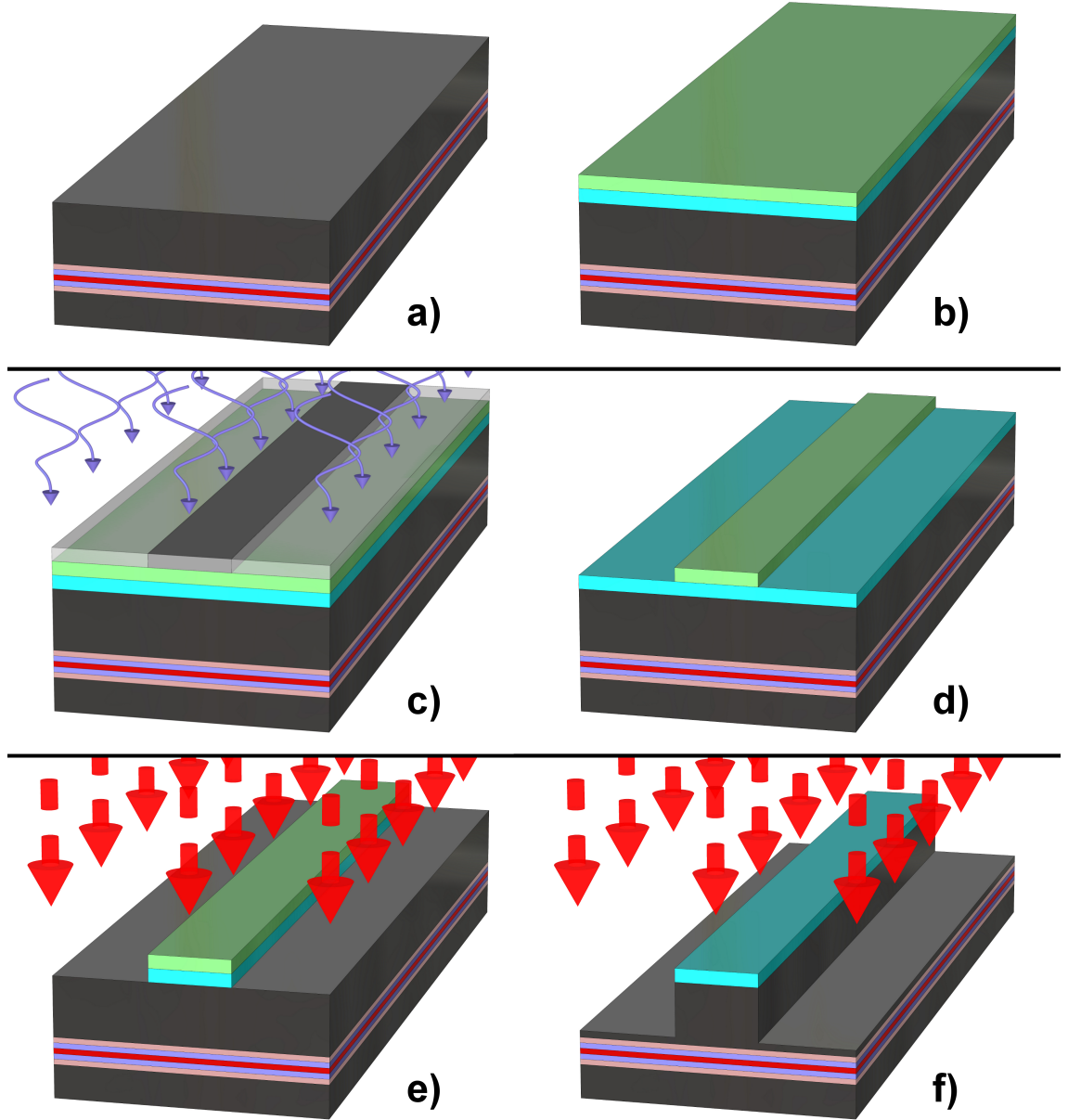
Figure 3.7 *Illustration of the RWG etching process steps. a) Plain laser wafer with the active region shown in red. b) Deposited layer of SiO_2 (teal) and spin-coated layer of positive photoresist (green). c) Application of a photolithography mask and UV exposure. d) Resist development. e) Plasma etching of the SiO_2 layer. f) Resist removal and plasma etching of the semiconductor.*

into bars (i.e. monolithic strips of semiconductor with multiple components side by side) and then individual components are detached from the bars. An illustration of the dicing steps is presented in figure 3.9.

The bars are separated from the wafer by cleaving. A small scratch is made to the
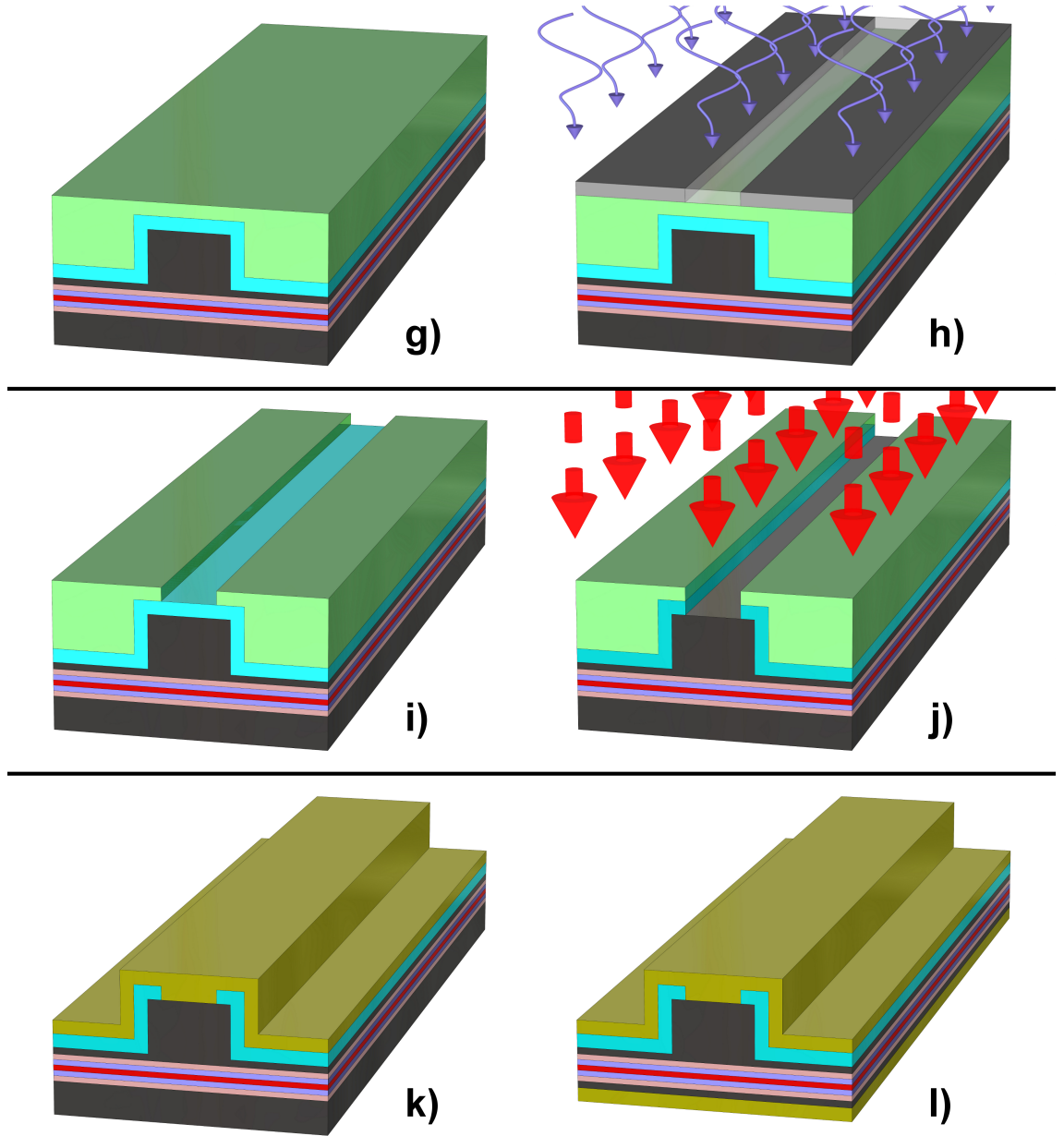
Figure 3.8 *Illustration of the opening and metallization process steps. g) Deposited layer of SiO$_2$ (teal) and spin-coated layer of positive photoresist (green). h) Application of photolithography mask and UV exposure. i) Resist development. j) Plasma etching of the SiO$_2$. k) Resist removal and p-metallization. l) Wafer thinning and n-metallization.*

desired position on the wafer and then strain is applied on the both sides of the scratch. This causes the wafer to split along a semiconductor crystal plane and the ends of the bar become smooth and straight. This is important since the light from a RWG laser or a SOA passes through the facet, and for the laser the facet provides the feedback necessary for lasing.

Individual components are separated from bars by making a scribe along component edges. The scribe is left a bit short from both bar facets so that they remain undamaged by the scribing needle.
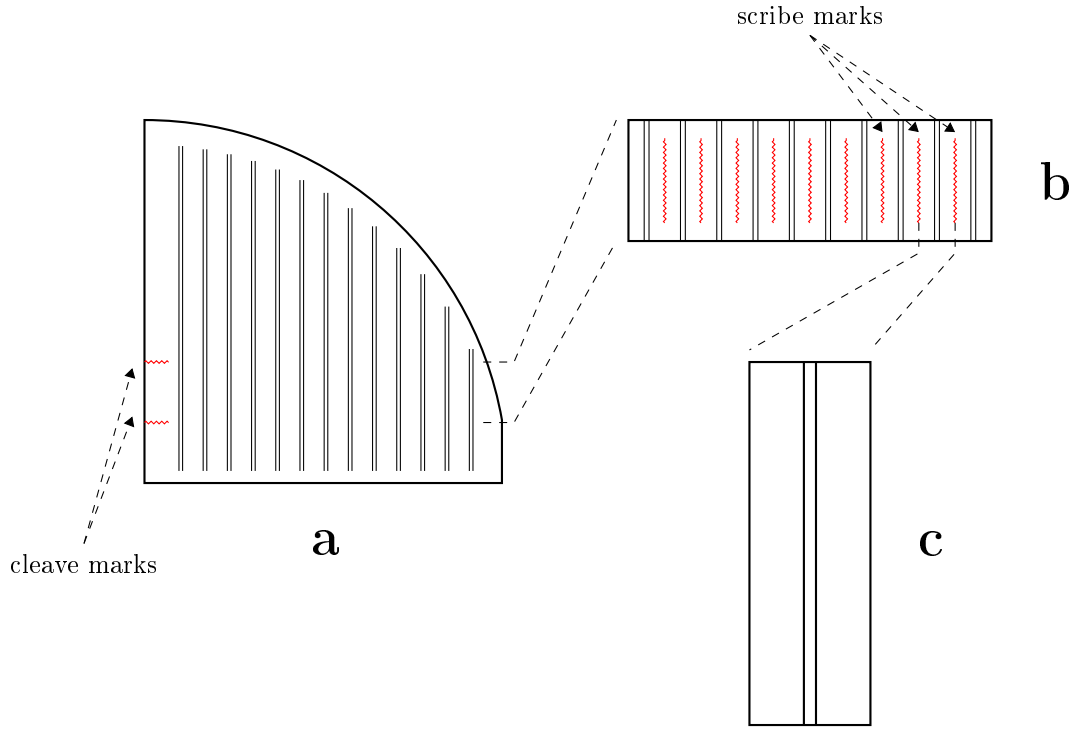
Figure 3.9 *Dicing steps. a) Quarter wafer after processing with ridge streets visible. Small cleave marks are made to the side. b) Bar cleaved from the wafer. Scribes are made between individual components just short from both facets. c) Individual chip scribed from the bar.*

Packaging

After the components are separated from the wafer they are attached to a submount to ease their handling and operation. This is called packaging or mounting. Components are attached to the submount usually using either a glue or a solder. Two basic types of packaging are p-up and p-down packaging.

In p-up packaging the component is attached to the submount from the n-side leaving the p-side up, and in p-down packaging the n-side is left up. The former

method is simpler since the component's active region is closer to the p-side and
the risk of the glue or solder short circuiting the component is smaller when the
p-side is further from the adhesive. On the other hand, p-down packaging leads
to better thermal management since the heat-producing active region is closer to
the submount and the heat doesn't have to pass through the substrate in order to
dissipate. A packaging robot is used for p-down packaging while p-up packaging can
be done by hand.

After attaching the chip to the submount either p-up or p-down, gold wires are
connected between the component's topside and an electrically insulated pad on the
submount. Thus the component can be operated by attaching electrical connectors
to the submount without the risk of damaging the chip. An illustration of a p-up
packaged chip is shown in figure 3.10.
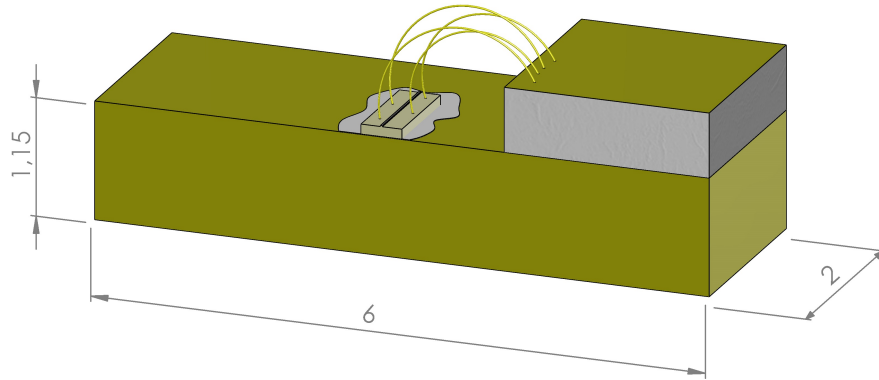
Figure 3.10 *Illustration of a component attached p-up to a SML2 submount using silver
epoxy glue. The component's p-side is connected with gold wires to the insulated pad on
the right. The dimensions are in millimeters.*

Antireflection coating

Antireflection (AR) coating is an essential step especially with SOA fabrication.
An as-cleaved GaAs facet reflects approximately 32% of light, which would provide
enough feedback to turn a RWG-SOA into a RWG laser. With AR coating this
reflectance can be reduced to near zero enabling travelling wave amplification.

An AR coating is a thin film deposited on the component's facet. It can either be single- or multi-layer, and the layers' refractive indices are between those of the substrate and the surrounding medium. With a single-layer AR coating the first reflection minimum occurs at a wavelength which corresponds to 1/4 of the optical thickness of the coating:

$$\lambda_{min(R)} = \frac{1}{4} t_f n_f, \tag{3.2}$$

where R is the reflectivity, t_f is the thickness of the film and n_f is the refractive index of the film, and the angle of incidence is assumed to be zero. The reduction in reflectance is caused by destructive interference of the reflections from the film surface and the substrate surface. The value of reflectance at its minimum is determined by the difference in the refractive indices of the substrate and the facet. The reflectance is zero if $n_f = \sqrt{n_s}$, with n_s being the substrate's refractive index. [29]

With multi-layer coatings the reflectivity can be reduced to zero even if the films have unideal refractive indices. Multiple layers also complicate the calculation of the reflectance, and methods such as the ray-transfer matrix method are needed to calculate the reflection of a multi-layer structure [30]. The layer structures used in this thesis were simulated using Essential Macleod simulation software.

Typical materials for AR coating are dielectrics such as SiO_2, SiN_x, TiO_2 and Al_2O_3. Deposition methods include e-beam evaporation, PECVD and atomic layer deposition (ALD).

In this thesis, AR coating was used to increase the threshold current of the RWG lasers that were used in the analysis. This was done because the method described in subsection2.4.1 uses the threshold current densities of the measured samples to find the g–J dependence, and higher threshold currents enable the discovery of gain values at higher current densities. The coating method employed in this thesis was ALD.

3.2 Characterization

After the components have been fabricated they are characterized to evaluate their quality. Different characterization methods give insight into different parts of the fabrication process. Typical aspects that are assessed are the semiconductor layer

structure design, the surface geometry design, fabrication process parameters and the packaging of the components.

Characterization may be performed either on packaged devices or directly from a laser bar. The advantages of bar probing is that many components can be measured quickly and clearly defective devices can be sorted out before packaging. The drawbacks include e.g. worse thermal management due to the lack of proper heat-sinking that packaging provides.

The characterization performed on the packaged components in this thesis was done using ORC's LDC5000 laser diode characterization system. The system has the capability to perform ILV, spectral and far field measurements in both continuous wave (CW) and pulsed modes.

Bar characterization was done with Modulight Inc's bar prober by Mr. Petri Melanen. The available measurement types were ILV, spectral and far field in CW mode.

3.2.1 ILV measurement

ILV (current, optical power and voltage) measurement determines the component's light output power and operating voltage as functions of the injection current. The component is driven with a range of currents and the output power from one facet and the voltage are measured for each current point. An idealized ILV curve is shown in figure 3.11.

The output power can be measured e.g. with an integrating sphere and a photodiode. The sphere is placed in front of the component and the photodiode is attached to a port on the side of the sphere. The advantages of using a sphere instead of measuring directly with a photodiode are that the sphere diffuses the light from the component and can collect most of the light emitted, thus reducing the variation in measurement results caused by different beam shapes. The main drawback is that the sphere attenuates the light thus increasing the minimum detectable power. Before measuring actual samples the system needs to be calibrated with a reference light source whose output power and wavelength are known. This is necessary so that the attenuation caused by the sphere and the wavelength dependence of the photodetector can be taken into account.

The preferred way to measure the voltage is to use a four-terminal measurement
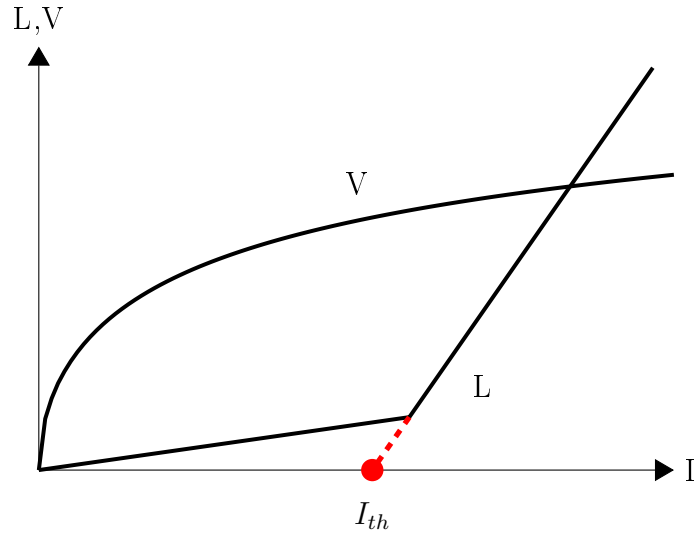
Figure 3.11 *Schematic of an ideal ILV curve of a RWG laser with the definition of the threshold current I_{th} shown.*

setup depicted in figure 3.12. If the voltage is measured as close to the component as possible, the voltage difference caused by the resistance in the current injection cables and especially the connectors is excluded from the measurement.
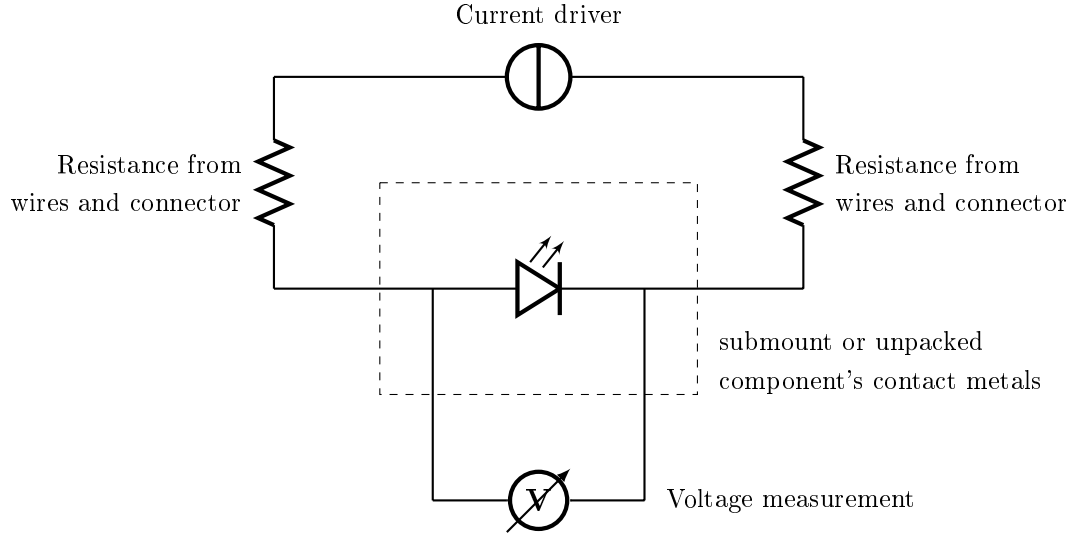
Figure 3.12 *Four-terminal sensing setup. Measuring the voltage as close as possible to the component's contact metals prevents the voltage difference caused by the resistance in the current injection system from being included in the measurement.*

Most of the parameters required for the analysis in this thesis are derived from ILV measurements. These include the threshold current, the slope efficiency and the voltage as a function of injection current density.

The threshold current I_{th} is defined to be the intersection between the extension of the L–I-curve above threshold and the I-axis [3]. This is shown in figure 3.11. In practice, the I_{th} can be calculated from unideal data using for example one of the three following methods:

- **Second order derivative:** The IL-curve is differentiated twice, and the threshold is taken to be at the current with the highest value of the second order derivative. Since the ideal IL-curve consists of two line segments with the latter one having a steeper slope, the second order derivative should peak at the treshold. Noise in the data can cause this method to give false results but this can be mitigated by applying e.g. the moving average filter [31] on the data before doing the analysis. Output nonlinearity that may occur at higher currents can be filtered out by focusing only on the lower end of the current range by exluding datapoints with output power above some fixed percentage of the maximum output power. See figure 3.13a.

- **Two-segment fit:** With two-segement fit the threshold current is first approximated by the second order derivative method. Then a line is fitted to the segments below and above the approximate threshold using linear regression. Finally the threshold is taken to be located at the intersection between these two fitted lines. The advantage of this method is that it helps to eliminate offset, e.g. if the power reading at $0\,\mathrm{mA}$ is not $0\,\mathrm{mW}$. The drawback is that possible kinks or nonlinearity at high currents can easily cause error to the position of the intersection. See figure 3.13b.

- **Linear fit:** A set of datapoints is taken from the measurement data so that the power of the points is between some fixed levels P_{low} and P_{high}, for example $P_{low} = 0.1P_{max}$ and $P_{high} = 0.5P_{max}$. Then a line is fitted to the selected datapoints using linear regression, and I_{th} is taken to be located at the intersection of the line and the I-axis. By setting the value of P_{high} low enough the effect of nonlinearity at high currents can be mitigated but the method is vulnerable to kinks in the IL-curve. See figure 3.13c.

It's worth noting that only the linear fit method gives the threshold current according
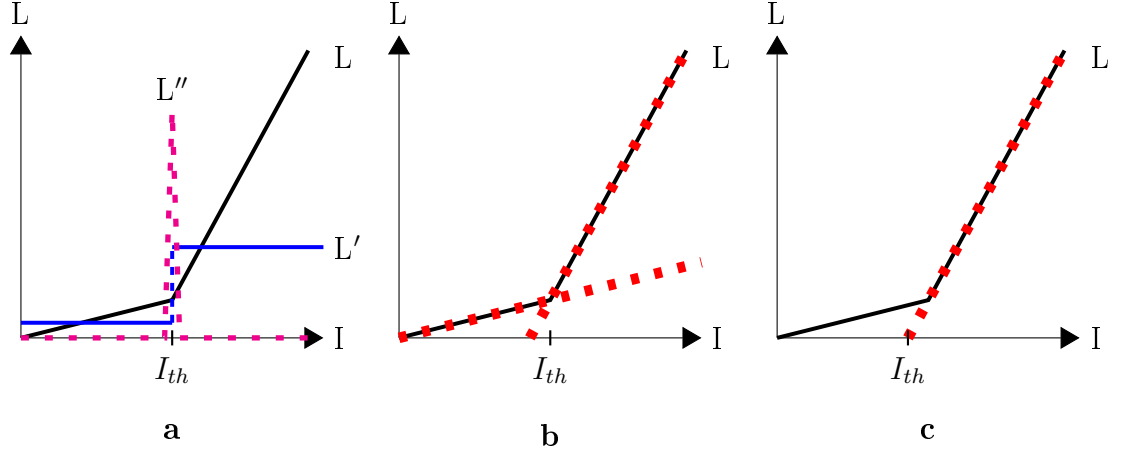
Figure 3.13 *Different ways to analyze the threshold current. a) Second order derivative method b) Two-segment fit c) Linear fit*

to the definition in [3] but based on experience the differences are usually small and mostly lost in the noise and nonlinearity of the actual data. In the analyses of this thesis, the threshold current is determined using the second order derivative method, and the datapoints from which the slope is calculated are limited to those with $P < 0.5P_{max}$.

The slope S can be calculated from the datapoints that lie above the threshold by fitting a line to the data using linear regression and taking the slope of the line as S.

3.2.2   Spectral measurement and far field measurement

Spectral measurement determines the distribution of the output light intensity as a function of the light's wavelength and far field (FF) measurement as a function of the output angle. In this thesis spectral measurement was used to determine the peak emission wavelength of the light of the RWG laser components since the gain in the corresponding SOAs is mainly in this wavelength range. FF measurements were used to select a suitable ridge width from the many component variants that were fabricated to find a component design whose FF stays as invariant as possible at different operating currents. A schematic picture of a typical FF is shown in figure 3.14.

Both the spectral and the FF measurements were performed by Modulight Inc.

using a bar prober. This way only components with suitable ridge width could be selected for packaging.
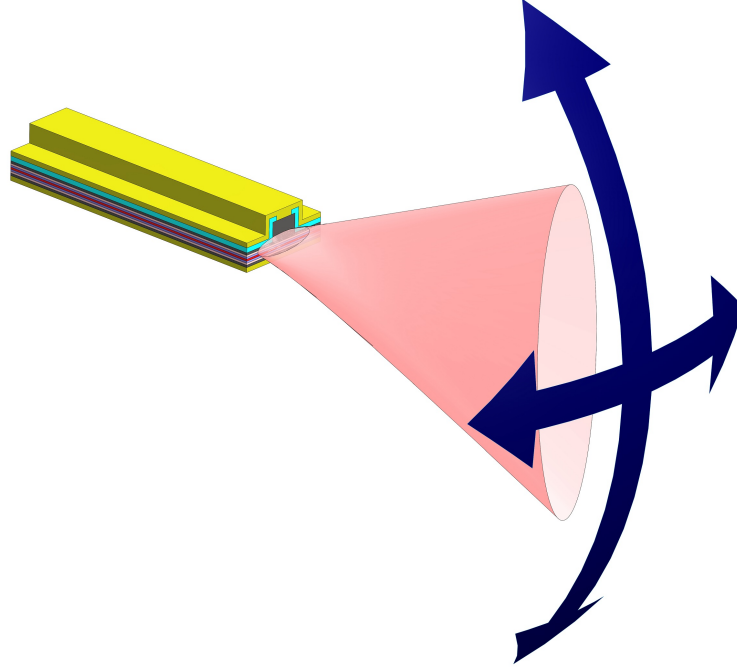
Figure 3.14 *Farfield of an RWG component. The output field is elliptical. At the component facet the field is elongated in the horizontal direction due to the dimensions of the active layer and the waveguide as well as the ridge geometry (see figure 2.5). Diffraction causes the field elongation to change direction away from the facet. In the far field the vertical (fast) axis is longer than the horizontal (slow) axis.*

3.3 Samples used in the analysis

The components fabricated for this thesis are RWG lasers. Six different variants made from the primary material with ridge widths 2.0 μm, 2.5 μm, 3.0 μm, 3.5 μm, 4.0 μm and 4.5 μm were chosen to find a width with optimal FF characteristics. The ridges ran over the whole wafer so that the component length could be chosen freely after the fabrication during cleaving. Each laser bar cleaved from the wafer contained 24 devices, four of each ridge width. The height of the ridges was measured to be 1119 nm using a profilometer.

The FF measurements done by Modulight Inc. from bars indicated that the ridge width 2.5 μm produced the most stable horizontal FF full width at half-maximum

(FWHM) when the operating current was changed. The experimentally determined FF FWHM variations are shown in figure 3.15. Because of this only components with ridge width 2.5 µm were used in the actual analysis.
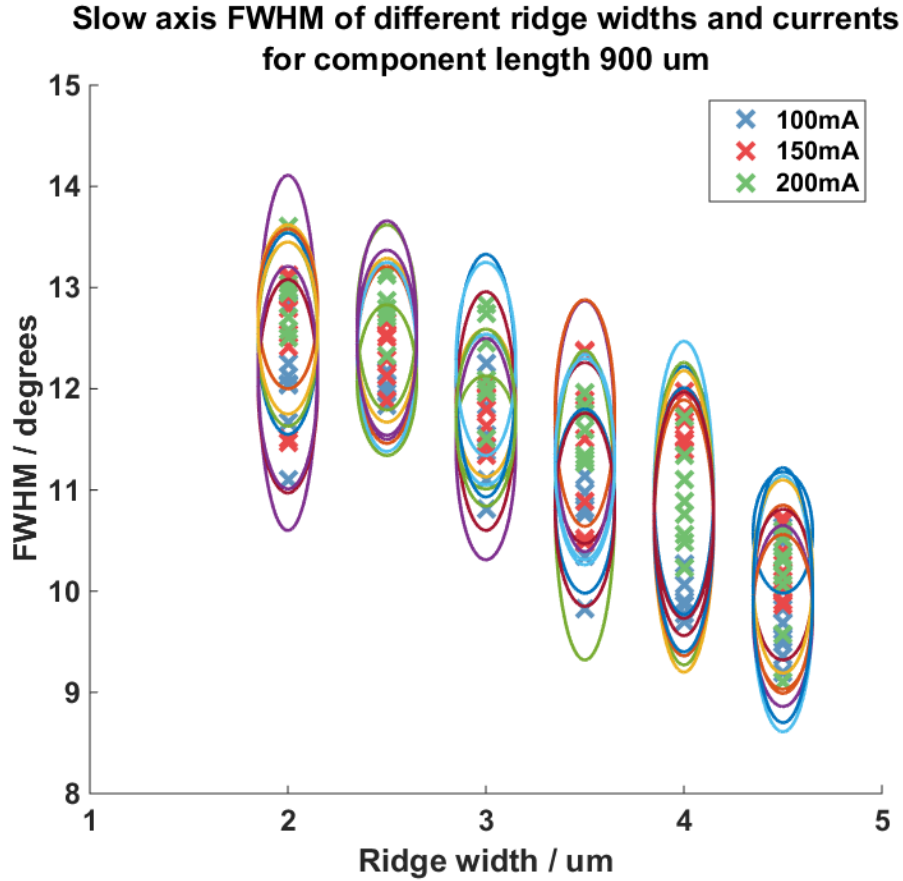
Figure 3.15 *Far field FWHM of* 900 µm *long components with different ridge widths operated at three different currents. Results from each individual component are surreounded by an oval: the more prolonged the oval is the more variation the FWHM exhibits when the current is changed. Ridge width* 2.5 µm *shows most stable FWHM.*

After the best ridge width was determined, four chips of each of the lengths 500 µm, 750 µm, 1000 µm, 1250 µm and 1500 µm were packaged and their ILV curves were measured at four different temperatures, 20 °C, 40 °C, 60 °C and 80 °C. After the measurements the chips were AR coated using ALD and measured again to obtain gain data at higher current densities. The coating used was a single Al_2O_3 layer grown by ALD which resulted in approximately 2.1 % facet reflectance. The reflectance was determined by a spectrophotometer measurement from a GaAs mon-

itor sample.

The components fabricated from the secondary material had a ridge width of 1.5 µm. The packaged component lengths were 500 µm, 725 µm, 950 µm, 1175 µm and 1400 µm. 11 components of the shortest length and five components of each of the other lengths were packaged. The components were characterized first without AR coating at different temperatures and then three different kinds of ALD-grown Al_2O_3 layers were coated on different components. The resulting facet reflections were approximately 5.1 %, 4.7 % and 1.8 %. The reflections were determined by spectrophotometer measurements from GaAs monitor samples.

Some packaged components from both materials performed poorly. The worst components were omitted from the analysis so that random damage incurred during fabrication or packaging wouldn't affect the results of the analysis.

4.   RESULTS AND ANALYSIS

This chapter reviews the acquired measurement data, the parameters used in the analysis of the data and the results of the analysis.

4.1   Measurement results

The measurement data used in the analysis of the primary and secondary material is presented in Tables B1 and B2 in appendix B respectively. Only data measured at $20\,°C$ is included.

4.2   Parameters and conditions for the analysis

Values for the parameters required for the analysis steps outlined in sections 2.3 and 2.4 have been collected in table 4.1 for the primary material and in table 4.2 for the secondary material along with an explanation how the value of each parameter was obtained.

***Table 4.1** Parameter values and their origin for the analysis of the primary material. Simulations were performed using LASTIP software by Crosslight Software Inc.*

Parameter	Symbol	Value	Source
Ridge width	w_{RWG}	$2.5\,\mu m$	Nominal RWG width in PL mask
Facet reflectance	R	0.32 or 0.021	as-cleaved or spectrophotometer measurement
Wavelength	λ	$1330\,nm$	Spectral measurement
Active area thickness	d	$14\,nm$	Nominal growth recipe thickness
Optical mode FWHM	w_{mode}	$1.7\,\mu m$	Simulation by Mr. Heikki Virtanen
Confinement factor	Γ	0.03	Simulation by Mr. Heikki Virtanen
Injection efficiency	η_{inj}	$52\,\%$	Simulation by Mr. Topi Uusitalo
Monom. rec. coeff	A	$10.5 \times 10^{8}\,s^{-1}$	[21]
Bimolec. rec. coeff	B	$1 \times 10^{-10}\,cm^3\,s^{-1}$	[21]
Auger rec. coeff	C	$4 \times 10^{-29}\,cm^6\,s^{-1}$	[21]

Table 4.2 *Parameter values and their origin for the analysis of the secondary material. Simulations were performed using LASTIP software by Crosslight Software Inc.*

Parameter	Symbol	Value	Source
Ridge width	w_{RWG}	1.5 µm	Nominal RWG width in PL mask
Facet reflectance	R	0.32, 0.051, 0.047, 0.018	as-cleaved or spectrophotometer measurement
Wavelength	λ	1560 nm	Spectral measurement
Active area thickness	d	28 nm	Nominal growth recipe thickness
Optical mode FWHM	w_{mode}	2.2 µm	Simulation by Mr. Topi Uusitalo
Confinement factor	Γ	0.058	Simulation by Mr. Topi Uusitalo
Injection efficiency	η_{inj}	32 %	Simulation by Mr. Topi Uusitalo
Monom. rec. coeff	A	$2.5 \times 10^8\,\mathrm{s}^{-1}$	[32]
Bimolec. rec. coeff	B	$4 \times 10^{-10}\,\mathrm{cm}^3\,\mathrm{s}^{-1}$	[32]
Auger rec. coeff	C	$5 \times 10^{-28}\,\mathrm{cm}^6\,\mathrm{s}^{-1}$	[32]

The application cases for the SOAs that this thesis focuses on present four different operating circumstances that have different input powers and amplification targets. These are presented in table 4.3. Since the input power and amplification target affect the required device length at a fixed injection current density, the optimal device length needs to be calculated separately for each application case.

Table 4.3 *Input powers, amplification targets and output powers for different SOA application cases.*

Case	SOA Input power	Amplification target	Output Power
1	−7 dBm / 0.200 mW	7 dB	0 dBm / 1.00 mW
2	−12 dBm / 0.063 mW	13 dB	1 dBm / 1.26 mW
3	−12 dBm / 0.063 mW	18 dB	6 dBm / 3.98 mW
4	−14 dBm / 0.040 mW	15 dB	1 dBm / 1.26 mW

4.3 Analysis results

This section presents the analysis results for both the primary and the secondary materials. First the dependence of voltage on the current density is described. Then the gain curve is presented. Finally the optimal device length for each application case is calculated.

4.3.1 Primary material

To obtain the dependence of voltage on the current density for the primary material, ILV measurements made from uncoated chips were used. The *I–V* curves were

Voltage as a function of current density, measured from components with different length
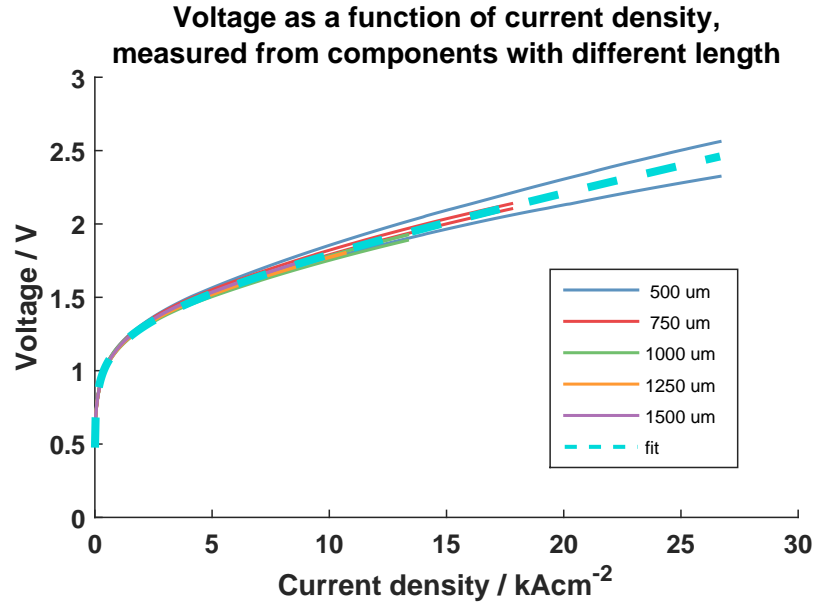
Figure 4.1 Dependence of voltage on injection current density for the primary material at 20 °C.

Threshold current density vs threshold modal gain and a logarithmic fit
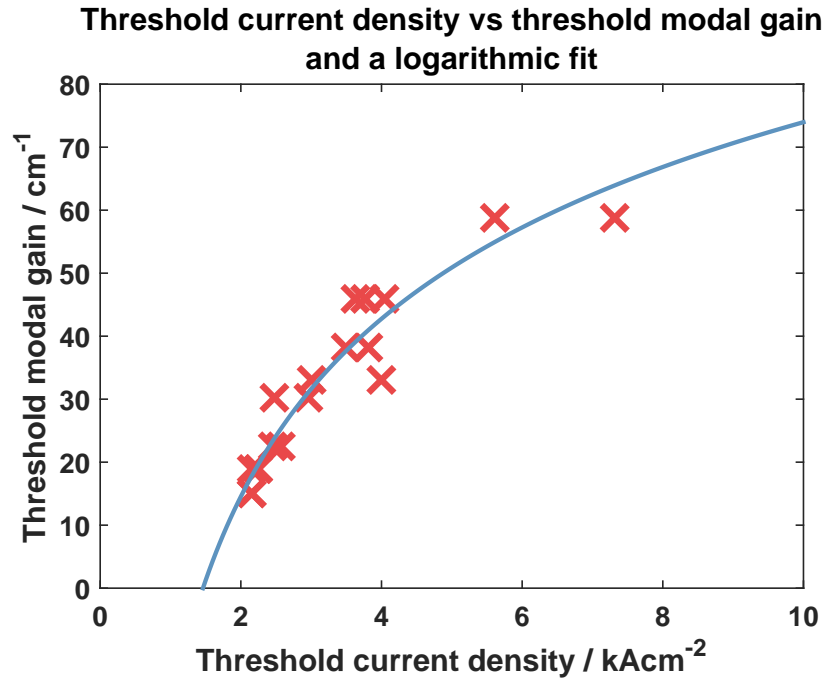
Figure 4.2 Dependence of the threshold modal gain on the threshold current density for the primary material at 20 °C.

transformed into $J-V$ curves, and a function described in equation 2.22 was fitted to the data. This was done separately for all of the different temperatures since the voltages were temperature-dependent. The $J-V$ data and the fit for $T = 20$ °C can be seen in figure 4.1.

The dependence of modal gain on current density $g_m(J)$ was calculated from ILV measurements of components with different lenghts and facet reflectances using the theory presented in subsection 2.4.1. This was done separately for all of the different temperatures. The datapoints with $T = 20\,°C$ and a fit calculated using the function 2.13 is shown in figure 4.2. The fitted $g_m(J)$ function is used both to determine the modal gain and the differential gain for equation 2.5. The internal quantum efficiency of the components was $39\,\%$ and the internal losses $7.4\,cm^{-1}$.

Table 4.4 *Optimal component length and power consumption for each application case for the components fabricated from the primary material at different temperatures.*

T	Case	Optimal component length	Power consumption
20 °C	#1	500 µm	71 mW
	#2	919 µm	131 mW
	#3	1288 µm	195 mW
	#4	1088 µm	150 mW
40 °C	#1	641 µm	89 mW
	#2	1189 µm	163 mW
	#3	1618 µm	242 mW
	#4	1380 µm	188 mW
60 °C	#1	803 µm	128 mW
	#2	1500 µm	236 mW
	#3	2028 µm	343 mW
	#4	1723 µm	271 mW
80 °C	#1	957 µm	195 mW
	#2	1767 µm	360 mW
	#3	2458 µm	514 mW
	#4	2024 µm	414 mW

Finally the power consumption of SOAs with different lengths was calculated for each of the targets presented in table 4.3 at different temperatures. The results are presented in table 4.4. The dependence of the injection current density, operating voltage and power consumption as functions of component length at $20\,°C$ are shown for the application cases one and three in figure 4.3. In the application case one the input power is high but the amplification low, and in the application case three the input power is low but the amplification high, so these two cases represent the behaviour of the SOAs in very different operation circumstances.
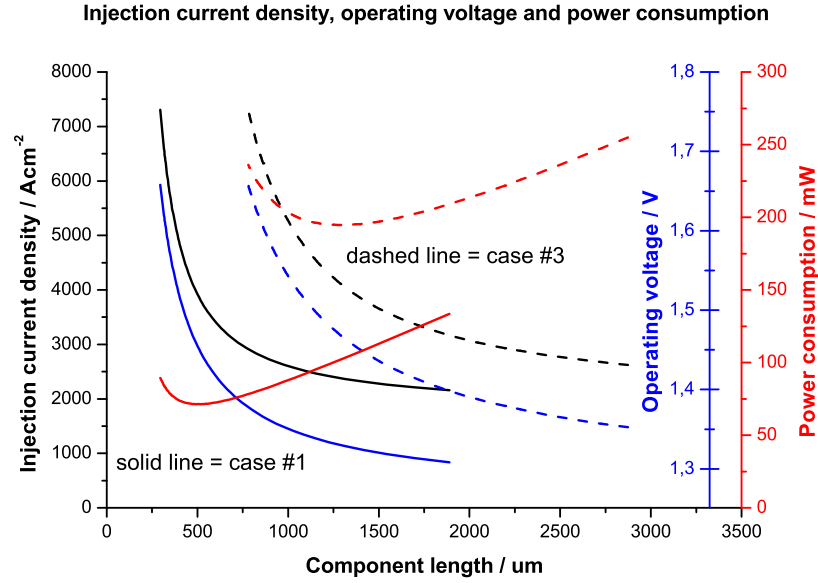
Figure 4.3 *Injection current density, operating voltage and power consumption as functions of the component length for the application cases one and three for components fabricated from the primary material at 20 °C. Case one is presented in solid line and case three in dashed line.*

4.3.2 Secondary material

The analysis of the secondary material was performed in the same way as the analysis of the first material. The internal quantum efficiency was 65 % and the internal losses 9.2 cm^{-1}. The J–V data and fit for $T = 20\,°C$ are shown in figure 4.4, the J–g_m data and fit for $T = 20\,°C$ in figure 4.5 and the optimal lengths and power consumptions for the application cases in table 4.5. Figure 4.6 shows the injection current, operating voltage and power consumption curves of components with different lengths.
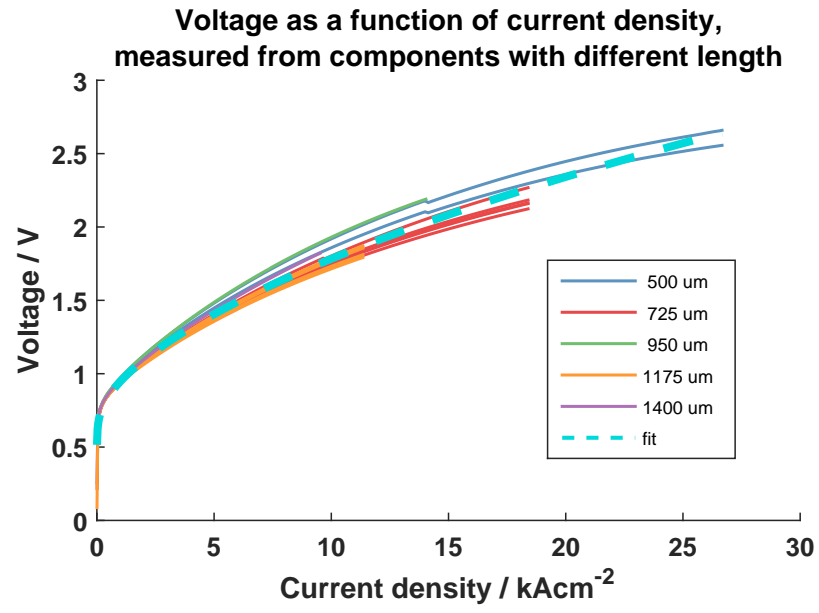
Figure 4.4 *Dependence of voltage on injection current density for the secondary material at 20 °C.*

Figure 4.5 *Dependence of the threshold modal gain on the threshold current density for the secondary material at 20 °C.*

Table 4.5 *Optimal component length and power consumption for each application case for the components fabricated from the secondary material at different temperatures.*

T	Case	Optimal component length	Power consumption
20 °C	#1	649 µm	32 mW
	#2	1210 µm	57 mW
	#3	1631 µm	91 mW
	#4	1381 µm	65 mW
40 °C	#1	700 µm	43 mW
	#2	1327 µm	77 mW
	#3	1793 µm	121 mW
	#4	1560 µm	89 mW
60 °C	#1	802 µm	60 mW
	#2	1496 µm	110 mW
	#3	2060 µm	167 mW
	#4	1749 µm	126 mW
80 °C	#1	871 µm	89 mW
	#2	1687 µm	163 mW
	#3	2325 µm	242 mW
	#4	1936 µm	187 mW

Figure 4.6 *Injection current density, operating voltage and power consumption as functions of the component length for the application cases one and t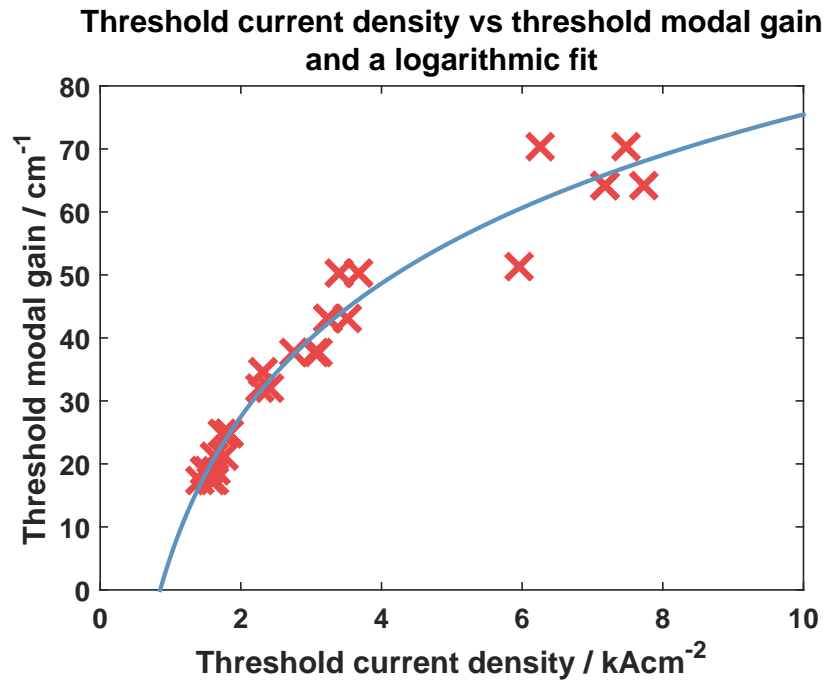hree for components fabricated from the secondary material at* 20 °C*. Case one is presented in solid line and case three in dashed line.*

5. SUMMARY

This section summarizes the work done, points out problems met, and suggests prospective improvements to the methods used.

5.1 Conclusions

The aim of this thesis was to analyze semiconductor optical amplifiers and to develop a systematic method to determine optimal component lengths in order to minimize the power consumption while meeting a predetermined amplification target. Only the component length was optimized, and e.g. the semiconductor layer structure and device fabrication process were taken as-is.

The developed method was used to study four different application cases. In each case, two different materials were compared: a novel material with GaInNAsSb QWs emitting around 1300 nm and a material resembling those used in standard communication lasers with AlGaInAs QWs emitting around 1550 nm.

The analysis was performed by fabricating RWG lasers with the same geometry as the intended SOAs would have and characterizing their ILV curves. In order to calculate the power consumption of a SOA with a certain length, three parameters were needed:

- The dependence of the operating voltage on the injection current density,

- the dependence of the modal gain on the injection current density and

- the dependence of the saturation power on the injection current density.

The J–V relationship was determined by measuring the ILV curves of the RWG components with different lengths, transforming the injection currents into injection

current densities using known ridge widths and component lengths, and finally fitting a curve to the datapoints using the least squares method.

The saturation power and carrier lifetime were solved using simulated optical field widths, confinement factors and current injection efficiencies and by taking the values of the recombination coefficients from literature.

The dependence of the modal gain on the injection current density was established by measuring the threshold currents and slope efficiencies of RWG lasers with different lengths. Additionally, AR coating was applied to the components using ALD to obtain gain data at even higher injection current densities.

After the parameters were solved as functions of the injection current density, the differential equation representing the light amplification inside the SOA could be used to calculate the required component lengths for a sampling of injection current densities. A figure of the calculation flow is shown in figure 5.1. In each application case the power consumption had a minimum at one component length, and the optimal components operated inside the injection current density range that was reached by the modal gain measurements, so the J–g_m data didn't have to be extrapolated.
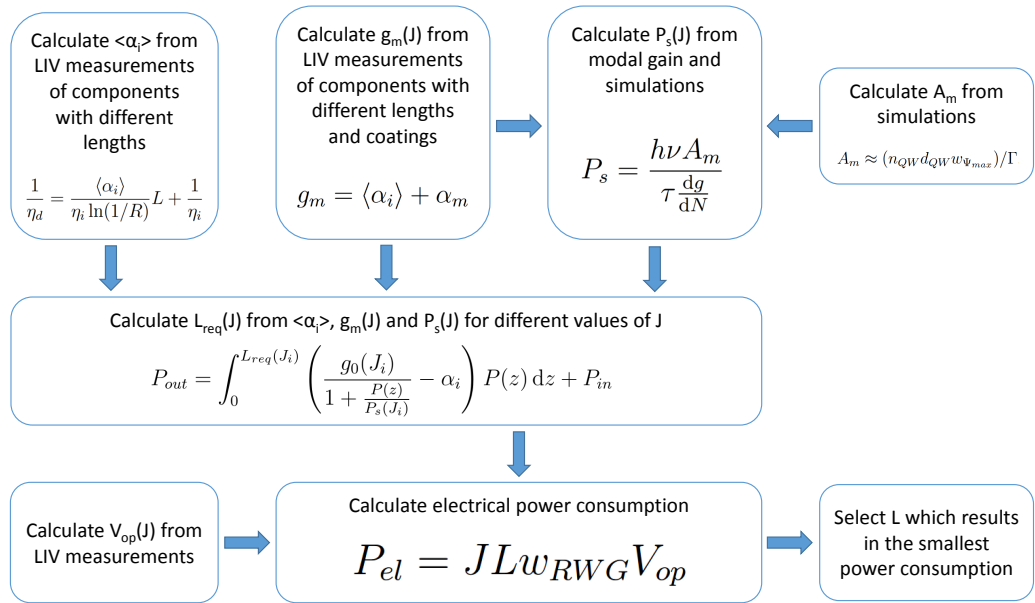
Figure 5.1 *Procedure to find the SOA length which results in the smallest power consumption.*

The primary material didn't show as good high-temperature characteristics as was expected. For example in the application case three, when temperature was increased from 20 °C to 80 °C, the power consumption of the primary material increased from 195 mW to 514 mW, while the power consumption of the secondary material increased from 91 mW to 242 mW. Even though the percentual increase of the primary material (164 %) was about the same as with the secondary material (166 %), the absolute increase of the primary material was 168 mW more making it a poor choice for high-temperature operation.

Overall, the power consumption of the components fabricated from the primary material was much higher than the power consumption of the components fabricated from the secondary material. The main reason for this seems to be that especially at low injection current densities the secondary material has much more gain, as can be seen from Figures 4.2 and 4.5. This enables the operation of the components fabricated from the secondary material at lower injection current densities which leads to a lower operating voltage, further decreasing the power consumption.

In addition to analyzing the primary and secondary materials in the four application cases of this thesis, the analysis method and the software developed can be used in the future to analyze new materials and component designs.

5.2   Issues observed

Two major problems were met during the work on this thesis. Firstly, the RWG lasers fabricated from the primary material had a very poor lifetime and their operation deteriorated noticeably during the characterization. This caused differences between the devices if some components had to be measured multiple times and when the components were measured for the second time after the AR coating.

The second issue was that the $J–g_m$ relationship didn't at first seem logarithmic as equation 2.13 suggests, especially with the primary material. Only after the components were AR coated and gain data was obtained at significantly higher injection current densities the logarithmic behaviour became apparent. This made designing the AR coating difficult since it was challenging to estimate how small reflectances would provide the most useful theshold current densities. For example, the selected AR coatings resulted in too low reflectances for most the shortest RWG lasers to operate.

5.3 Future work

Some of the greatest sources of uncertainty in the results were the determination of the carrier lifetime and the saturation power. In this thesis their calculation was based on simulations and values obtained from literature. Especially the literature values may lead to significant inaccuracy since references for exactly the same structures that were used in the thesis were not found.

In the future, it should be possible to determine both the carrier lifetime and the saturation power empirically, e.g. using a SOA to amplify a pulsed signal and measuring the time-dependent output power.

Otherwise, the accuracy of the results could be improved by fabricating and packaging more components, and applying AR coatings of different reflectances. This would increase the covered injection current density range and reduce the variation caused by random defects in the RWG components.

BIBLIOGRAPHY

[1] FP7-ICT-2013-11 project proposal RAPIDO (619806): Revolutionary Advances in Photonics Integration Being Applied for Optical Communication. Description of Work: Part B, 2013.

[2] I Vurgaftman, JR Meyer, and LR Ram-Mohan. Band parameters for III–V compound semiconductors and their alloys. *Journal of applied physics*, 89(11):5815–5875, 2001.

[3] Larry A Coldren, Scott W Corzine, and Milan L Mashanovitch. *Diode lasers and photonic integrated circuits*, volume 218. John Wiley & Sons, 2012.

[4] CS Wang and BM Klein. First-principles electronic structure of Si, Ge, GaP, GaAs, ZnS, and ZnSe. i. self-consistent energy bands, charge densities, and effective masses. *Physical Review B*, 24(6):3393, 1981.

[5] Albert G Baca and Carroll IH Ashby. *Fabrication of GaAs devices*. Number 6. IET, 2005.

[6] Pirjo Leinonen. *Techniques for Semiconductor Laser Processing*. PhD thesis, Tampere University of Technology, 2007.

[7] Peter Van Zant and Chapman. *Microchip fabrication: a practical guide to semiconductor processing*, volume 5. McGraw-Hill New York, 2000.

[8] Ali Rostami, Hamed Baghban, and Reza Maram. *Nanostructure Semiconductor Optical Amplifiers: Building Blocks for All-optical Processing*. Springer Science & Business Media, 2010.

[9] Toshiaki Suhara. *Semiconductor laser fundamentals*. CRC Press, 2004.

[10] Terji Durhuus, Benny Mikkelsen, Carsten Joergensen, Soeren Lykke Danielsen, and Kristian E Stubkjaer. All-optical wavelength conversion by semiconductor optical amplifiers. *Lightwave Technology, Journal of*, 14(6):942–954, 1996.

[11] Kristian E Stubkjaer. Semiconductor optical amplifier-based all-optical gates for high-speed optical processing. *Selected Topics in Quantum Electronics, IEEE Journal of*, 6(6):1428–1435, 2000.

[12] Niloy K Dutta and Qiang Wang. *Semiconductor optical amplifiers.* World scientific, 2013.

[13] Luis Borruel, Helena Odriozola, José MG Tijero, Ignacio Esquivias, Slawomir Sujecki, and Eric C Larkins. Design strategies to increase the brightness of gain guided tapered lasers. *Optical and Quantum Electronics*, 40(2-4):175–189, 2008.

[14] AI Onischenko, KA Williams, AB Massara, JCL Yong, JM Rorison, Richard V Penty, and JH White. Feasibility of AlGaInAs lasers for high speed uncooled communication systems. In *Lasers and Electro-Optics Europe, 2000. Conference Digest. 2000 Conference on*, pages 1–pp. IEEE, 2000.

[15] Sandra R Selmic, Tso-Min Chou, JiehPing Sih, Jay B Kirk, Art Mantle, Jerome K Butler, David Bour, and Gary A Evans. Design and characterization of 1.3-μm AlGaInAs-InP multiple-quantum-well lasers. *Selected Topics in Quantum Electronics, IEEE Journal of*, 7(2):340–349, 2001.

[16] Minko Balkanski and Richard Fisher Wallis. *Semiconductor physics and applications*, volume 8. Oxford University Press, 2000.

[17] Won-Jin Choi, P Daniel Dapkus, and Jack J Jewell. 1.2-μm GaAsP/InGaAs strain compensated single-quantum-well diode laser on GaAs using metal-organic chemical vapor deposition. *Photonics Technology Letters, IEEE*, 11(12):1572–1574, 1999.

[18] Joel Salmi. Metalloinnin erikoiskysymyksiä. Master's thesis, 2014.

[19] GE Stillman, CM Wolfe, and JO Dimmock. Hall coefficient factor for polar mode scattering in n-type GaAs. *Journal of Physics and Chemistry of Solids*, 31(6):1199–1204, 1970.

[20] G Eisenstein, N Tessler, U Koren, JM Wiesenfeld, G Raybon, and CA Burrus. Length dependence of the saturation characteristics in 1.5-μm multiple quantum well optical amplifiers. *Photonics Technology Letters, IEEE*, 2(11):790–791, 1990.

[21] Robin Fehse, Stanko Tomić, Alfred R Adams, Stephen John Sweeney, Eoin P O'Reilly, Aleksey Andreev, and Henning Riechert. A quantitative study of radiative, Auger, and defect related recombination processes in 1.3-μm GaInNAs-based quantum-well lasers. *Selected Topics in Quantum Electronics, IEEE Journal of*, 8(4):801–810, 2002.

[22] Nils W Carlson. Design considerations and operating characteristics of high-power active grating-surface-emitting amplifiers. *Quantum Electronics, IEEE Journal of*, 28(9):1884–1893, 1992.

[23] John R Arthur. Molecular beam epitaxy. *Surface science*, 500(1):189–217, 2002.

[24] Processing image reversal resists. `http://www.microchemicals.com/technical_information/image_reversal_resists.pdf`. Accessed: 2016-03-14.

[25] AZ6600-series: Thermally stable positive resists. `http://www.microchemicals.com/products/photoresists/az_6612.html`. Accessed: 2016-03-14.

[26] M Nishiguchi, Noboru Goto, Takeshi Sekiguchi, Hideaki Nishizawa, Hideki Hayashi, and Kimizo Ono. Mass production back-grinding/wafer-thinning technology for GaAs devices. *Components, Hybrids, and Manufacturing Technology, IEEE Transactions on*, 13(3):528–533, 1990.

[27] RO Carlson, GA Slack, and SJ Silverman. Thermal conductivity of GaAs and GaAs(1-x)Px laser semiconductors. *Journal of Applied Physics*, 36(2):505–507, 1965.

[28] CJ Glassbrenner and Glen A Slack. Thermal conductivity of silicon and germanium from 3 K to the melting point. *Physical Review*, 134(4A):A1058, 1964.

[29] E Hecht and A Zajac. *Optics*. Addison-Wesley, 1979. Fourth printing.

[30] Klaus Halbach. Matrix representation of gaussian optics. *Am. J. Phys*, 32(2):90, 1964.

[31] The scientist and engineer's guide to digital signal processing. `http://www.dspguide.com/pdfbook.htm`. Accessed: 2016-04-11.

[32] TJ Houle, JCL Yong, CM Marinelli, S Yu, JM Rorison, IH White, JK White, AJ SpringThorpe, and B Garrett. Characterization of the temperature sensitivity of gain and recombination mechanisms in 1.3-μm AlGaInAs MQW lasers. *Quantum Electronics, IEEE Journal of*, 41(2):132–139, 2005.

APPENDIX A. EXPLICIT SOLUTIONS FOR CARRIER LIFETIME CALCULATION

The equation for carrier lifetime τ in subsection2.4.2 is

$$\tau = \frac{1}{A + BN_{th} + CN_{th}^2} \tag{A1}$$

$$\tau = \frac{1}{A + B(\frac{\eta_{inj}\tau}{qd}J) + C(\frac{\eta_{inj}\tau}{qd}J)^2}, \tag{A2}$$

where A is the monomolecular recombination coefficient, B the bimolecular recombination coefficient, C the Auger recombination coefficient, η_{inj} the injection efficiency, q the charge of the carriers, d the thickness of the active region and J the injection current density. When solved with Matlab symbolic toolbox, the results for the equations are

$$\tau(J) = \begin{cases} T(J) \\ T_+(J) \\ T_-(J) \end{cases} \tag{A3}$$

with

$$T = \left(\sqrt{\left(\frac{d^2\,q^2}{2\,C\,J^2\,\eta_{inj}^2} - \frac{B^3\,d^3\,q^3}{27\,C^3\,J^3\,\eta_{inj}^3} + \frac{A\,B\,d^3\,q^3}{6\,C^2\,J^3\,\eta_{inj}^3} \right)^2 + \left(\frac{A\,d^2\,q^2}{3\,C\,J^2\,\eta_{inj}^2} - \frac{B^2\,d^2\,q^2}{9\,C^2\,J^2\,\eta_{inj}^2} \right)^3} \right.$$
$$\left. + \frac{d^2\,q^2}{2\,C\,J^2\,\eta_{inj}^2} - \frac{B^3\,d^3\,q^3}{27\,C^3\,J^3\,\eta_{inj}^3} + \frac{A\,B\,d^3\,q^3}{6\,C^2\,J^3\,\eta_{inj}^3} \right)^{\frac{1}{3}}$$
$$- \frac{\frac{A\,d^2\,q^2}{3\,C\,J^2\,\eta_{inj}^2} - \frac{B^2\,d^2\,q^2}{9\,C^2\,J^2\,\eta_{inj}^2}}{\left(\sqrt{\left(\frac{d^2\,q^2}{2\,C\,J^2\,\eta_{inj}^2} - \frac{B^3\,d^3\,q^3}{27\,C^3\,J^3\,\eta_{inj}^3} + \frac{A\,B\,d^3\,q^3}{6\,C^2\,J^3\,\eta_{inj}^3} \right)^2 + \left(\frac{A\,d^2\,q^2}{3\,C\,J^2\,\eta_{inj}^2} - \frac{B^2\,d^2\,q^2}{9\,C^2\,J^2\,\eta_{inj}^2} \right)^3} + \frac{d^2\,q^2}{2\,C\,J^2\,\eta_{inj}^2} - \frac{B^3\,d^3\,q^3}{27\,C^3\,J^3\,\eta_{inj}^3} + \frac{A\,B\,d^3\,q^3}{6\,C^2\,J^3\,\eta_{inj}^3} \right)^{\frac{1}{3}}}$$
$$- \frac{B\,d\,q}{3\,C\,J\,\eta_{inj}} \tag{A4}$$

$$
T_{\pm} = \cfrac{\dfrac{A\,d^2\,q^2}{3\,C\,J^2\,\eta_{inj}^2} - \dfrac{B^2\,d^2\,q^2}{9\,C^2\,J^2\,\eta_{inj}^2}}{2\left(\sqrt{\left(\dfrac{d^2\,q^2}{2\,C\,J^2\,\eta_{inj}^2} - \dfrac{B^3\,d^3\,q^3}{27\,C^3\,J^3\,\eta_{inj}^3} + \dfrac{A\,B\,d^3\,q^3}{6\,C^2\,J^3\,\eta_{inj}^3}\right)^2 + \left(\dfrac{A\,d^2\,q^2}{3\,C\,J^2\,\eta_{inj}^2} - \dfrac{B^2\,d^2\,q^2}{9\,C^2\,J^2\,\eta_{inj}^2}\right)^3} + \dfrac{d^2\,q^2}{2\,C\,J^2\,\eta_{inj}^2} - \dfrac{B^3\,d^3\,q^3}{27\,C^3\,J^3\,\eta_{inj}^3} + \dfrac{A\,B\,d^3\,q^3}{6\,C^2\,J^3\,\eta_{inj}^3}\right)^{\frac{1}{3}}}
$$

$$
- \cfrac{\left(\sqrt{\left(\dfrac{d^2\,q^2}{2\,C\,J^2\,\eta_{inj}^2} - \dfrac{B^3\,d^3\,q^3}{27\,C^3\,J^3\,\eta_{inj}^3} + \dfrac{A\,B\,d^3\,q^3}{6\,C^2\,J^3\,\eta_{inj}^3}\right)^2 + \left(\dfrac{A\,d^2\,q^2}{3\,C\,J^2\,\eta_{inj}^2} - \dfrac{B^2\,d^2\,q^2}{9\,C^2\,J^2\,\eta_{inj}^2}\right)^3} + \dfrac{d^2\,q^2}{2\,C\,J^2\,\eta_{inj}^2} - \dfrac{B^3\,d^3\,q^3}{27\,C^3\,J^3\,\eta_{inj}^3} + \dfrac{A\,B\,d^3\,q^3}{6\,C^2\,J^3\,\eta_{inj}^3}\right)^{\frac{1}{3}}}{2} - \dfrac{B\,d\,q}{3\,C\,J\,\eta_{inj}}
$$

$$
\pm \cfrac{\sqrt{3}\,\mathrm{i}\left(\dfrac{A\,d^2\,q^2}{3\,C\,J^2\,\eta_{inj}^2} - \dfrac{B^2\,d^2\,q^2}{9\,C^2\,J^2\,\eta_{inj}^2}\right)}{\left(\sqrt{\left(\dfrac{d^2\,q^2}{2\,C\,J^2\,\eta_{inj}^2} - \dfrac{B^3\,d^3\,q^3}{27\,C^3\,J^3\,\eta_{inj}^3} + \dfrac{A\,B\,d^3\,q^3}{6\,C^2\,J^3\,\eta_{inj}^3}\right)^2 + \left(\dfrac{A\,d^2\,q^2}{3\,C\,J^2\,\eta_{inj}^2} - \dfrac{B^2\,d^2\,q^2}{9\,C^2\,J^2\,\eta_{inj}^2}\right)^3} + \dfrac{d^2\,q^2}{2\,C\,J^2\,\eta_{inj}^2} - \dfrac{B^3\,d^3\,q^3}{27\,C^3\,J^3\,\eta_{inj}^3} + \dfrac{A\,B\,d^3\,q^3}{6\,C^2\,J^3\,\eta_{inj}^3}\right)^{\frac{1}{3}}}{2}}
$$

$$
\pm \cfrac{\sqrt{3}\,\mathrm{i}\left(\sqrt{\left(\dfrac{d^2\,q^2}{2\,C\,J^2\,\eta_{inj}^2} - \dfrac{B^3\,d^3\,q^3}{27\,C^3\,J^3\,\eta_{inj}^3} + \dfrac{A\,B\,d^3\,q^3}{6\,C^2\,J^3\,\eta_{inj}^3}\right)^2 + \left(\dfrac{A\,d^2\,q^2}{3\,C\,J^2\,\eta_{inj}^2} - \dfrac{B^2\,d^2\,q^2}{9\,C^2\,J^2\,\eta_{inj}^2}\right)^3} + \dfrac{d^2\,q^2}{2\,C\,J^2\,\eta_{inj}^2} - \dfrac{B^3\,d^3\,q^3}{27\,C^3\,J^3\,\eta_{inj}^3} + \dfrac{A\,B\,d^3\,q^3}{6\,C^2\,J^3\,\eta_{inj}^3}\right)^{\frac{1}{3}}}{2}
$$

$$\tag{A5}$$

With reasonable values for the parameters A, B, C, d, q, η and J, the solutions $T_{\pm}$ have an imaginary part and their real parts are negative, while the solution T is real-valued and positive. Thus, solution T is taken to represent the carrier lifetime.

APPENDIX B. MEASUREMENT RESULTS

Table B1 *Facet reflectivities, threshold currents and slopes at 20 °C for the components fabricated from the primary material*

L (µm)	R	I_{th} (mA)	S (W/A)
500	0.32	31	0.1437
500	0.32	37	0.1338
750	0.32	46	0.1272
750	0.32	48	0.1192
750	0.021	105	0.1114
750	0.021	137	0.1077
1000	0.32	54	0.1138
1000	0.32	56	0.1175
1000	0.32	56	0.1157
1000	0.021	94	0.1303
1000	0.021	91	0.1290
1000	0.021	101	0.1225
1250	0.021	119	0.1185
1250	0.021	109	0.1188
1500	0.32	81	0.0918
1500	0.32	81	0.0939
1500	0.021	150	0.1105
1500	0.021	113	0.1213

Table B2 *Facet reflectivities, threshold currents and slopes at 20 °C for the components fabricated from the secondary material*

L (µm)	R	I_{th} (mA)	S (W/A)
500	0.32	17	0.1730
500	0.32	18	0.1696
500	0.047	47	0.1664
500	0.047	56	0.1563
725	0.32	20	0.1608
725	0.32	19	0.1669
725	0.32	20	0.1671
725	0.32	20	0.1676
725	0.32	19	0.1653
725	0.018	78	0.1418
725	0.018	84	0.1457
725	0.018	78	0.1300
725	0.051	40	0.1799
725	0.051	37	0.1828
950	0.32	25	0.1557
950	0.32	23	0.1514
950	0.018	85	0.1422
1175	0.32	27	0.1421
1175	0.32	27	0.1386
1175	0.32	29	0.1296
1175	0.32	26	0.1421
1175	0.32	26	0.1426
1175	0.018	62	0.1629
1175	0.018	57	0.1712
1175	0.018	57	0.1719
1175	0.051	41	0.1763
1175	0.051	41	0.1725
1400	0.32	30	0.1318
1400	0.32	34	0.1087
1400	0.32	33	0.1079
1400	0.018	58	0.1711
1400	0.018	65	0.1650
1400	0.018	64	0.1606